Tornadoes in the Tyrrhenian regions of the Italian peninsula: the case study of 28 July 2019

Elenio Avolio[a,*], Mario Marcello Miglietta[b]

[a] *National Research Council of Italy, Institute of Atmospheric Sciences and Climate (CNR-ISAC), Lamezia Terme, Italy*

[b] *National Research Council of Italy, Institute of Atmospheric Sciences and Climate (CNR-ISAC), Padua, Italy*

Abstract

On 28 July 2019 a tornado affected a small rural area in central Italy causing several damages and one casualty. The tornado was spawned by a thunderstorm embedded in a linear convective system that crossed the central Tyrrhenian Sea. The environment was characterized by high values of convective available potential energy (CAPE) and deep layer wind shear (DLS). The severity of this type of events highlights the importance of carrying out multi-scale integrated analysis on tornado phenomena in the Italian central Tyrrhenian area, one of the most affected by these events and on which dedicated studies have not yet been carried out so far.

Tornadoes in the area are identified in the years 1990-2021, allowing to perform a synoptic/mesoscale analysis of the main patterns associated to these events. The 30-year analysis is carried out using both radiosonde observations and ERA5 reanalysis.

The average synoptic configuration is dominated by an upper level trough over the central Mediterranean Sea and by a low surface pressure area over northwestern Italy, with southwesterly upper-level winds over the Tyrrhenian Sea and higher-than-average northwesterly winds entering the western Mediterranean through the gulf of Lion. Moderate mean values of CAPE (about 700 J Kg^{-1}) and DLS (about 15 m s^{-1}) are found, and the linear shape of the hodograph suggests favorable conditions for multicell systems.

High-resolution WRF (Weather Research and Forecasting) model simulations of the 28 July 2019 case study correctly reproduced the event and the structure of the storm. Extreme values of the typical instability parameters/indices denote an environment particularly favorable for tornado formation; some sensitivity tests permitted to evaluate the role of several forcing (Sea Surface Temperature, surface fluxes and orography) in the development and the trajectory of the storm.

Keywords: Tornado; Italy; WRF; ERA5; severe storms; convective environment; synoptic patterns.

1. Introduction

Tornadoes are recognized as one of the most severe meteorological phenomena, mainly affecting the midlatitudes (Goliger and Milford, 1998). Their occurrence and intensity are assessed based on visual observations and post-event reports, which lead to subsequent classifications (e.g., Enhanced Fujita scale, EF hereafter; Doswell et al., 2009).

For many years, detailed studies about these phenomena have been almost exclusively confined to the USA, due to the higher frequency and intensity compared to other countries (Brooks et al., 2003). However, recent studies (Antonescu et al., 2016, 2017) demonstrated the high frequency and damage potential of tornadoes in several European countries (Dotzek, 2003; Taszarek et al., 2020).

The methodology of analysis is generally based on instability parameters identified in radiosounding profiles. Several studies, both for US (Rasmussen and Blanchard, 1998; Craven and Brooks, 2004) and for Europe (Giaiotti et al., 2007; Groenemeijer and van Delden, 2007; Taszarek et al., 2013; 2017), showed, in agreement with theoretical studies (e.g., Rotunno, 1981; Weisman and Klemp, 1986), that large vertical wind shear, high convective available potential energy (CAPE), low lifting condensation level (LCL) are ingredients that favor the formation of significant tornadoes. The main difference between US and Europe events is in the higher values of these

parameters in the former region.
Other studies considered numerical model atmospheric reanalysis (Brooks et al. 2003; Gensini and Ashley 2011; Taszarek et al., 2020; Romero et al., 2007; Ingrosso et al., 2020; Rodríguez and Bech, 2020); also in these works useful thresholds for specific severe weather parameters were identified, helping weather forecasters to recognize potential tornadic storm environments. Reanalysis data have the advantage of incorporating upper-air observations, satellite data, surface measurements, and they have a finer spatial/temporal resolution compared to the sparse radiosonde locations. Even if the agreement between rawinsondes and reanalyses should be better explored (Pilguj et al., 2022), in particular to understand if the reanalyses are capable of correctly reproducing the fine-scale atmospheric thermodynamic and kinematic vertical profiles, such gridded data have the great advantage to reproduce the main synoptic patterns and the mesoscale fields that may be potentially related to extreme weather events, such as tornadoes.

Although the impact of Italian tornadoes on the territory is not negligible (Groenemeijer and Kuhne, 2014), the scientific literature on this topic is very limited. After the pioneering climatological work of Palmieri and Pulcini (1978), and the historical survey by Gianfreda et al. (2005), relative to south-eastern Italy, Giaiotti et al. (2007) proposed a first climatology of the Italian tornadoes and waterspouts, that was updated after a decade by Miglietta and Matsangouras (2018).
Other studies mainly focused on severe tornado case studies able to cause significant damages, injuries and even fatalities. Miglietta and Rotunno (2016) and Miglietta et al. (2017a; 2017b) analyzed in detail a multi-vortex EF3 tornado occurred in southeastern Italy, and Zanini et al. (2017) performed a study on a rare EF4 tornado affecting Veneto region. More recently, Avolio et al. (2020) analyzed a severe convective storm affecting northwestern Italy, plausibly related to a tornado coexisting with a downburst. Finally, Avolio and Miglietta (2021) studied four tornado-spawning supercells over southern Italy, hitting the same (Ionian) regions and characterized by common synoptic conditions.
Two recent studies dealt with the synoptic/mesoscale conditions favorable to Italian tornadoes. Ingrosso et al. (2020) studied the mesoscale environmental characteristics related to a selection of 57 significant tornadoes occurring over Italy in the 2000–2018 years, analyzing the role of the vertical wind shear and of CAPE derived from reanalysis fields. They performed a punctual investigation, using the fields extracted at the grid point nearest to the tornado locations, to conclude that large vertical wind shear and medium-to-high values of CAPE are possible precursors of tornadoes. Bagaglini et al. (2021) analyzed synoptic patterns and mesoscale parameters derived from reanalysis in the same period, selecting 149 tornadoes over Italy. They performed a cluster analysis, describing the main characteristics of the environment favorable to tornadoes for the different Italian areas.

In the present work, first we examine the main synoptic patterns and upper-air environmental characteristics associated to tornado events over a specific Italian area, i.e. the central peninsular Tyrrhenian regions, but using a larger tornado database (32-years period, from 1990 to 2021), so that a larger number of tornado events are retained over Italy (459), and in the central Tyrrhenian regions in particular (93). Also, differently from the previous works, in the present study we consider not only reanalysis fields but also upper-air observations (from a sounding station representative of the study area). Note that this is the first study dealing with tornadoes in this Italian region.
In the second part of the work, we focus on a significant tornado, representative of the intense vortices occasionally affecting this area, through high-resolution numerical simulations performed with the Weather Research and Forecasting (WRF) model. The tornado occurred in Fiumicino (west of Rome) on 28 July 2019, and caused one casualty and several damages.
The characteristics of the storm spawning the tornado suggest it was a Quasi-Linear Convective System (QLCS; Weisman and Davis, 1998). Previous works about QLCS-related tornadoes have

shown significant differences with respect to those related to isolated supercell (SPC) thunderstorms, which are generally stronger and with clearer radar signatures and to which a larger number of studies has been devoted.

In the US, the first climatology of QLCS tornadoes (Tessendorf and Trapp, 2000; Trapp et al., 2005) demonstrated that they account for about 20% of the total cases, and that they were predominantly weak and more frequent in winter and during nighttime. A recent study (Ashley et al., 2019), based on 22-year radar image classification and machine learning methods, demonstrate that more than 21% of tornadoes are due to QLCSs across the central and eastern US.

In Europe, Gatzen (2011) analyzed 10 years of QLCSs during the cold season in Germany, finding that they were mostly associated with weak convective instability and strong low-level vertical wind shear. Clark (2013) examined 7 years of convective storms in the UK, finding that 27% of the QLCSs produced at least one tornado; Mulder and Schultz (2015) assessed that QLCSs are responsible for 42% of tornado days. The analysis of some tornadoes in Spain (Ramis et al., 1997; Aran et al., 2009; Bech et al., 2011) demonstrated that tornadoes were predominantly associated to multicell storms and linear systems, rather than to single cell thunderstorms.

Thus, higher percentages of tornadoes related to QLCSs appear in Europe compared with the US, possibly due to differences in the environmental conditions, and several authors emphasized the importance of studying (for forecasting and surveillance purposes) also these types of events, although potentially less intense: Bech et al. (2015) studied a QLCS in NE Spain producing a weak (EF0/EF1) tornado; Buckingham and Schultz (2020) documented 9 tornado outbreaks related to QLCSs in the UK between 2004 and 2019, through a synoptic-scale approach.

The paper is organized as follow. The data used to analyze the 30-yr period, the observational and modeling tools used in this work are described in Section 2. Section 3 presents the results; first, the main synoptic/mesoscale characteristics related to the tornadoes in the central Tyrrhenian regions; then, the high-resolution numerical model simulations of this particular case study. Section 4 summarizes the main results of the work.

2. Data and methods

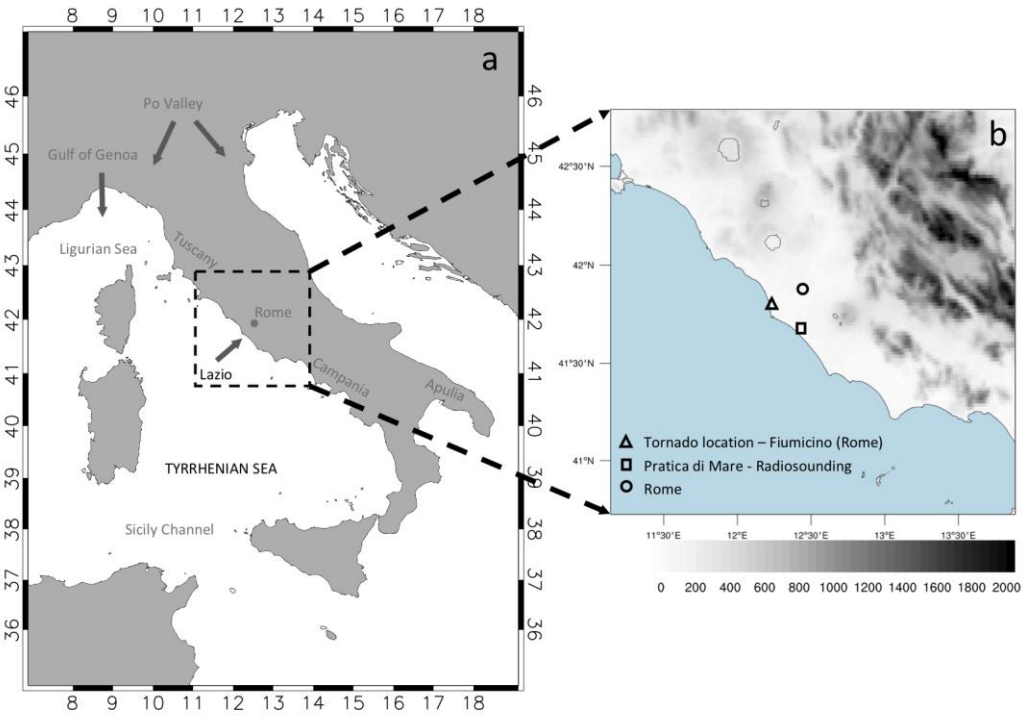

Fig. 1. The main locations cited in the text. On the right: 1 km grid spacing WRF model inner domain and terrain height (m).

The positions of the tornado and other cited locations are also reported.

2.1 ESWD reports

For the climatological part of our study, we used the European Severe Weather Database (ESWD; Dotzek et al., 2009), which aims to collect and provide quality-controlled information on severe convective storm events over Europe. The database has been widely used and successfully adopted in several research activities and publications during the years, and the structure of the reports permits to perform some selections aimed at increasing the reliability of the considered reports.
First, we select the tornado events occurred in Italy from 1990 to 2021 (1848 reports); in the following we will refer to "30-years period" when we indicate the complete database.
To avoid unreliable events and weak cases, we retain:
- Only reports with quality control level 1 (report confirmed by reliable source) or 2 (scientific case study);
- Only events classified with Fujita scale equal to 1 or higher;
- Only tornadoes over land (thus excluding waterspouts);
- Only reports with maximum time accuracy of 3 hours (-1.5h / +1.5h) and location accuracy less than 3 km.

This selection allowed retaining 445 events over Italy, of which 93 events cover the central Tyrrhenian regions (Figure 1; Tuscany, Lazio and Campania regions, considering the tornadoes occurred on their west side). These criteria are restrictive since they led to a conspicuous decrease of the initial database. However, these choices make it possible to consider all and only the significant events with high spatial-temporal plausibility.

2.2 Upper air radiosonde observations

Upper air RAdiosonde OBservation (RAOB) from Global Telecommunications System (GTS) reports at Pratica di Mare (Lazio region, see position in Fig. 1b) were considered, as this site is the only valuable one for the central peninsular Tyrrhenian regions; this profile is particularly useful for the case study analyzed in section 3.2, since it is very close to the location where the tornado was observed.
The sounding data relative to the selected 93 events were considered to evaluate the atmospheric conditions during the tornadoes, and to calculate specific instability parameters with the aim of comparing them with those calculated using the ERA5 reanalysis.
Sounding data were taken from the Department of Atmospheric Science, University of Wyoming archive, considering profiles only at 00 and 12 UTC. To make uniform the format of the soundings, we considered only the 18 mandatory pressure levels from the surface up to 5 hPa (https://glossary.ametsoc.org/wiki/Mandatory_level).
In addition to the wind, temperature, and humidity fields at the prescribed levels, the RAOB reports make available instability parameters that have been considered here: Convective Available Potential Energy (CAPE), Total Totals index (TT), and K index (KI) (see Table A1 for their definition).
Additionally, the deep layer wind shear (DLS; the differences between the wind vector near the surface (1000 hPa) and at about 6 km (500 hPa)), the 0-3 km storm relative helicity (SRH03) and the WMAXSHEAR were also calculated (Table A1).
Several methodologies are adopted to choose representative soundings for the study of severe weather events as tornadoes. In this work we followed a temporal proximity-inflow method employed, among others, by Rasmussen and Blanchard (1998), Rasmussen (2003), Renko et al. (2016) and Rodríguez and Bech (2017). Our temporal selection criteria considered a 9-h window, starting 6h before and ending 3h after each event; each sounding comprised in this time interval was retained (78 soundings, in our case). The asymmetry of the time window with respect to the time of tornado occurrence is due to the possible change in the environmental conditions after the passage

of the tornado. Of the 78 cases, 6 reports refer to two or more nearby events, while 9 soundings over 78 were not available. In summary, 63 proximity soundings were taken into account.

2.3 ERA5 ReAnalysis

The global climate monitoring dataset ECMWF ReAnalysis (ERA5; Hersbach et al., 2020) is considered here with two purposes: to study the large-scale atmospheric patterns related to the tornado occurrences, and to calculate the thermodynamic diagrams, the hodographs and specific sounding-derived parameters at the Pratica di Mare site coordinates, with the aim of comparing them with the analogous parameters derived from the RAOB observations.
The ERA5 fields are available hourly on a regular latitude-longitude grid with 0.25°×0.25° horizontal resolution; both "pressure-levels" (37 pressure levels, from the surface to 0.01 hPa) and "single-levels" databases are used here. The fields considered in this work are: geopotential height at 500 hPa (HGT500); temperature at 850 hPa (T850); mean sea level pressure (MSLP); U and V wind components at 500, 700, 900 hPa and at 10 m height; CAPE; TT; KI. These parameters were directly extracted from the ERA5 archive at 00 and 12 UTC, for a 30-years period (1990-2021), over a domain large enough to represent the main synoptic features influencing the Mediterranean area (i.e., −20°W, 20°S, 50°E, 60°N). Similar to what has been done for upper air observations, other fields/parameters were also calculated: DLS, SRH03 and WMAXSHEAR (Table A1).
The same temporal proximity-in flow method described in section 2.2 is adopted for the ERA5 data. Therefore, for the sake of punctual comparison with radiosounding profiles (section 3.1.1), 63 pseudo proximity soundings are evaluated in the same point. Instead, for the calculation of large-scale patterns analysis, the full set of 72 events is retained; for the calculation of the anomalies, the whole 30-year period ERA5 database was considered to define the average fields.

2.4 WRF model

The high-resolution simulation of the EF2 tornado case study is performed with the non-hydrostatic Advanced Research (ARW) Weather Research and Forecasting model (WRF) (Skamarock et al., 2019) version 4.2. Three two-way nested domains were configured with horizontal grid spacing of 9, 3 and 1 km respectively (Fig. 1b; Table 1).
In order to choose the "best" model set-up, first we qualitatively compared several WRF outputs (maximum composite reflectivity, vertical velocity and Updraft Helicity in particular; Table A1) with the observed radar reflectivity / lightning maps (Fig. 11), also considering the ESWD report. Several runs were executed to test different initial and boundary conditions and different initial times; further experiments were also conducted to study the impact of different physical parameterization schemes (PBL and radiation schemes). The results (not shown) indicate that the WRF simulation (CTL run in the following) forced with the ECMWF-IFS analysis/forecasts, with the configurations summarized in Table 1, was in better agreement with the observations. Starting from the CTL configuration, further specific sensitivity tests were done (see section 3.2.3 for the main results) in order to study the forcings affecting the evolution of the supercell.

RUN	RUN time and INIT	Domains	Physics
CTL	**Init** = ECMWF-IFS analysis/forecasts starting at 00 UTC on 27 July (16 vertical levels, from 1000 to 10 hPa; 0.1° resolution; step 3h) **Run** WRF= 21h (starting	**Grids** = 9 km (192 × 184 grid points), 3 km (193 × 181 grid points), 1 km (232 × 232 grid points) **WRF Vertical**	**PBL** = ACM2 (Pleim, 2007),) & **SF_SFCCLAY** = MM5 Similarity (Jimenez et al., 2012) **MP** = WSM 6-class (Hong et al., 2006) **CU** = BMJ (Janjic, 1994) for 9/3 km grids; explicit for 1 km grid **RA_LW** = RRTMG (Iacono et al., 2008) **RA_SW** = RRTMG (Iacono et al., 2008)

	at 06 UTC on 27 July)	**levels** = 40	**SF_SURFACE** = Noah Land Surface Model (Tewari et al., 2004)

Table 1 WRF model configuration (CTL run)

3. Results and discussion

3.1 Tornadoes in the Tyrrhenian regions of the Italian peninsula

A detailed climatological analysis over the whole Italy territory is out of the purposes of our paper, but we devote a few comments about it in Appendix B. In the present Section, in contrast, we focus on the environmental characteristics associated with the tornadoes in the central Tyrrhenian regions of the Italian peninsula (CT hereafter). As previously mentioned, the selection criteria described in section 2.1 allowed to retain 93 events in the CT regions, 52 of which refer to the Lazio region (Fig. 1).

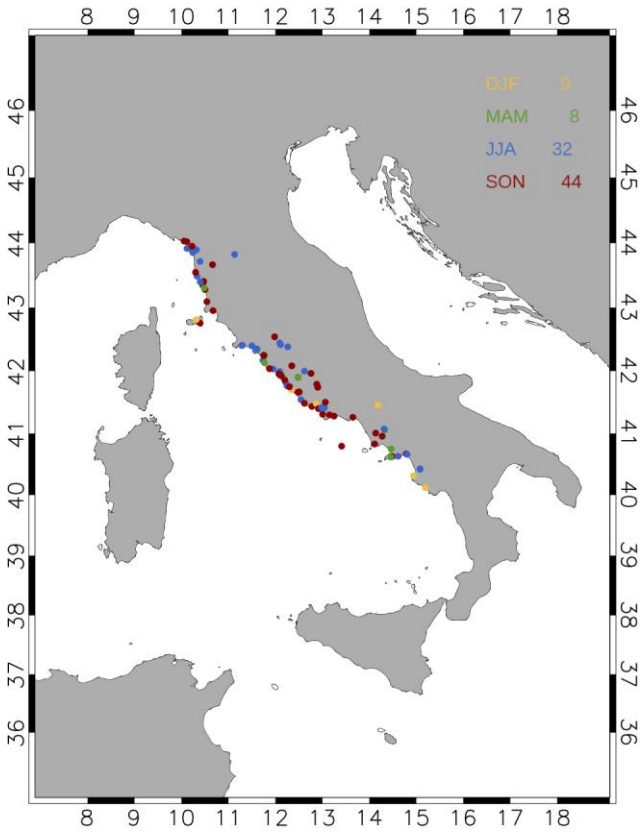

Fig. 2. Position of the 93 tornadoes during the 30-years period in the CT regions; the different colors refer to the different seasons.

The number of recorded tornadoes (Fig. 2) in autumn (September-October-November) appears noticeably greater than in other seasons (44 over a total of 93), with a high concentration on the western coasts of Lazio. The concentration of events near the coastline suggests an important role played by the sea, possibly tornadoes originated as waterspouts.
In the next sub-sections, we will analyze the main upper air atmospheric conditions and large-scale atmospheric patterns related to the 93 selected tornadoes occurred on CT.

3.1.1 Composite sounding-derived parameters at Pratica di Mare

In this section we evaluate the upper air atmospheric characteristics at the coordinates of Pratica di Mare (the only close upper air observation site; Fig. 1b), in terms of thermodynamic diagrams, hodographs and sounding-derived parameters, both considering observations (RAOB) and reanalysis fields (ERA5), for the selected 63 proximity soundings in the CT regions. For a fair comparison, the average sounding was calculated considering the mandatory pressure levels (18 levels) from the surface to 5 hPa (see section 2.2) for both RAOB and ERA5 data. The composite thermodynamic diagrams (skew-T diagrams) and hodographs are reported in figure 3; specific sounding-derived parameters were also calculated and are shown in figure 4.

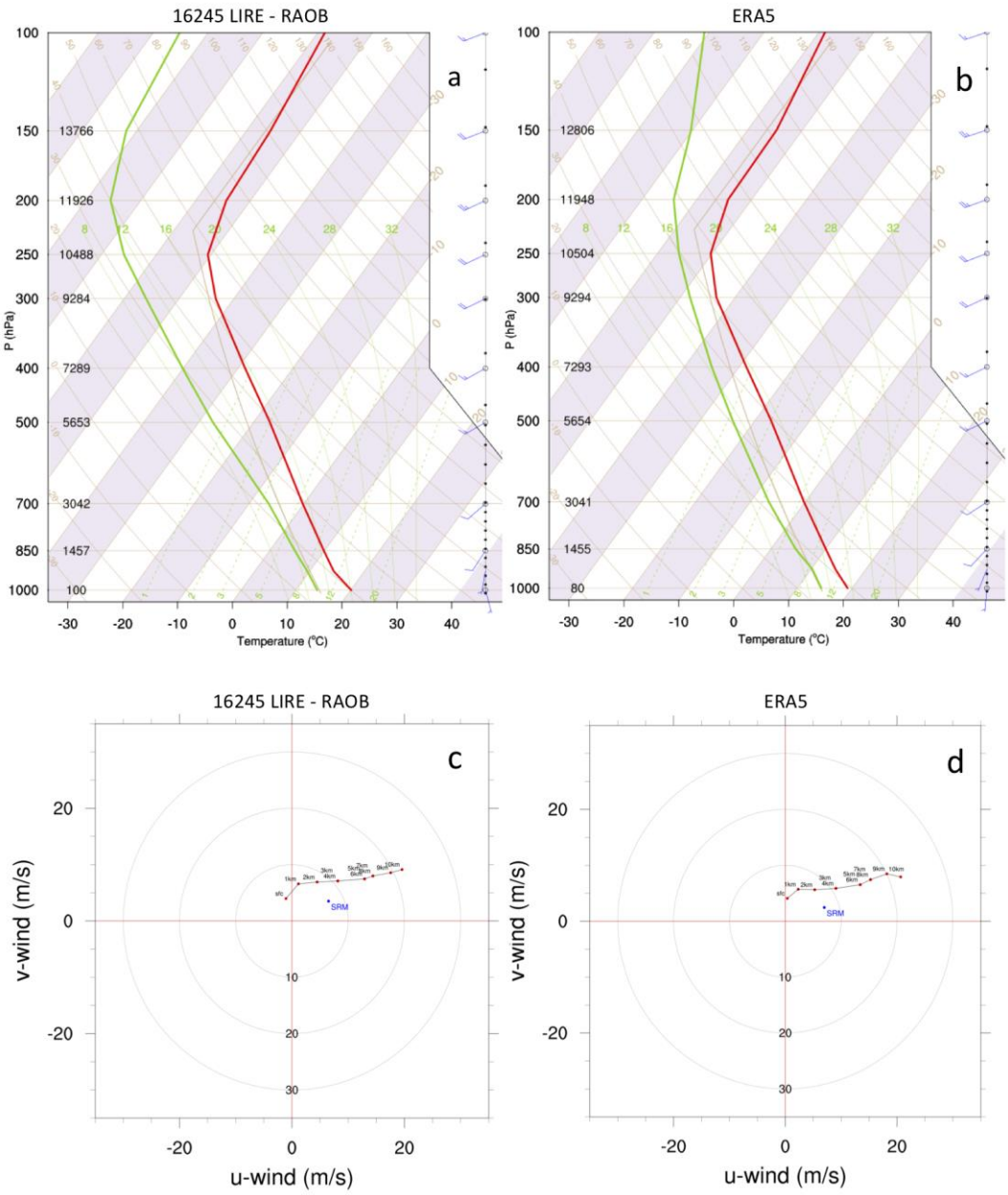

Fig. 3. Composite Skew-T diagrams and hodographs at Pratica di Mare from RAOB sounding (a,c) and from ERA5 reanalysis (b,d). (RAOB data Source: Department of Atmospheric Science, University of Wyoming).

The mean vertical profiles (very smooth due to the limited number of vertical levels we used) are shown in figure 3a-b for RAOB and ERA5 data, respectively, and indicate a general agreement. The ERA5 pseudo-soundings show higher humidity in the whole vertical column, particularly in the

low levels, thus represent potentially more unstable conditions. A moderate directional wind-shear is visible in the lower atmospheric layers (below 1500 m), due to weak-to-moderate south-southeasterlies near the surface that slightly intensify with height and become southwesterlies at 850 hPa. However, the rotation in the low-levels is more apparent in the RAOB data than in the ERA5 reanalysis.

Figure 4 shows the box-and-whiskers plots for the composite CAPE, KI, TT, DLS, WMAXSHEAR and SRH03 (Table A1); below the x-axis the mean values are also reported. The observed and simulated mean values of the most unstable CAPE (MUCAPE) are quite similar in RAOB and ERA5 and are of moderate intensity (616 J kg^{-1} for RAOB and 741 J kg^{-1} for ERA5). However, as discussed in Avolio and Miglietta (2021) and Miglietta et al. (2017a), a strong variability in CAPE may occur in the Mediterranean in a relatively short distance and time scale, thus these values may not be fully representative of the environmental conditions in which the supercells develop.

All the others sounding-derived parameters show a good agreement between observations and simulations. The mean values of KI and TT are almost identical for RAOB and ERA5 (KI is about 25 K and TT about 48 K, for both datasets). Also, the mean values of DLS are moderate, for both RAOB and ERA5, and in good agreement between them (15.1 m s^{-1} for RAOB and 14.6 m s^{-1} for ERA5). In contrast, a general underestimation of SRH03 is apparent in ERA5, with mean values almost halved compared to observations (137 m^2 s^{-2} for RAOB and 78 m^2 s^{-2} for ERA5). This may be a consequence of the smaller wind shear in the low levels (see the different wind direction near the ground in Figs 3a and 3b). Except for the SRH03, all variables reported in figure 4 show a satisfactory agreement also in terms of upper/lower extremes/quartiles and medians; however, for CAPE and DLS, the upper extremes in ERA5 data are higher than in RAOB. The mean values of the parameters are certainly greater than the average fields (see also ERA5 maps in section 3.1.2), although not extreme.

Also, we tested the hypothesis that these moderate values may be due to the low representativeness of the Pratica di Mare station for the whole region; thus we repeated the analysis only for the tornadoes occurred in the Lazio region (55 events and 33 useful proximity soundings). Although some composite values are slightly higher (e.g., CAPE of 802 J kg^{-1} for RAOB and 906 J kg^{-1} for ERA5; SRH03 159 m^2 s^{-2} for RAOB and 95 m^2 s^{-2} for ERA5), the wind shear values, as well as KI and TT, are very close to those obtained using the whole dataset. Therefore, we rejected our hypothesis.

The composite hodographs (figure 3c-d) show a very similar shape in the two cases (RAOB and ERA5), with moderate values of bulk shear. Mean southerlies are visible in the low levels and west-southwesterlies above; the storm relative motion is toward the right of the vertically averaged steering flow, following Corfidi et al. (1996) and Corfidi (2003). In this relatively straight hodograph, directional shear is noticeable only in the low levels. At upper levels the wind speed increases but the direction changes only slightly with height (unidirectional shear) favoring the formation of right-moving multicell systems, as pioneeringly assessed by Chisholm and Renick (1972) and Weisman and Klemp (1984). These types of multicell storms are generally regenerated by new cells, that are triggered on the flanks of older cells, which generally move following the mid-tropospheric winds (Wallace and Hobbs, 2006).

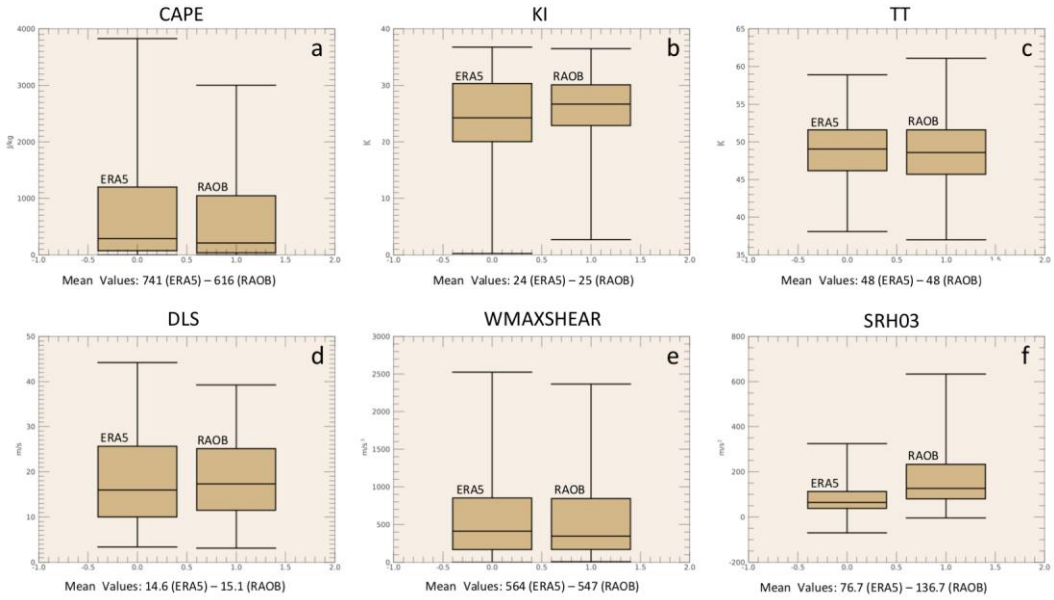

Fig. 4. Boxplots for CAPE (a), KI (b), TT (c), DLS (d), WMAXSHEAR (e) and SRH03 (f), for both ERA5 (box on the left) and RAOB (box on the right) data, related to the 63 selected proximity soundings. The 25th, the 50th (median) and the 75th percentiles are shown, as well as the extremes. Mean values are also reported on x-axis.

3.1.2 ERA5-derived meteorological and convective environments

To study the large-scale atmospheric patterns at the time of the tornadoes in the CT regions, the ERA5 anomaly fields are here reported in figure 5. We considered the HGT500, T850, MSLP and 10m wind fields; the anomalies were computed considering the difference between the fields averaged in the 72 selected events (see section 2.3) and the 30-year averages.

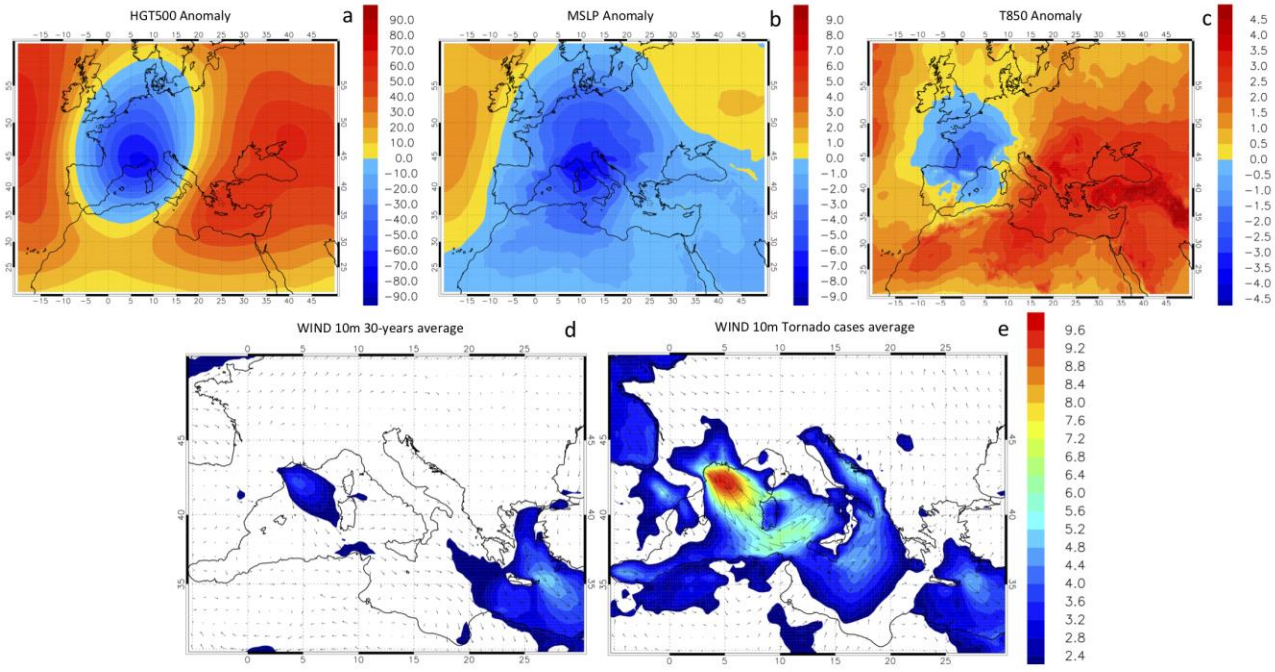

Fig. 5. Anomalies of the ERA5 fields of geopotential height at 500 hPa (m; (a)), mean sea level pressure (hPa; (b)), temperature at 850 hPa (K; (c)). Anomalies are calculated considering the mean values of the selected 72 tornado cases with respect to a 30-year period average (1990–2021). The 10-m wind (vector and speed; m/s) are reported for the 30-years average (d) and for the 72-tornado

cases average (e). *(For interpretation of the references to colour in this figure legend, and all the others in the manuscript, the reader is referred to the web version of this article).*

The synoptic configuration can be summarized as follows:
a) Considering the HGT500 anomalies (Fig. 5a), a deeper-than-average upper-level trough is centered over the northwestern Italy, just north of the Gulf of Genoa.
b) All the northern Italian regions are affected by lower-than-average mean sea level pressure (Fig. 5b), with values smaller than 8 hPa with respect to the mean; this suggests the occurrence of a typical synoptic configuration for this area, i.e. a cyclogenesis over the Gulf of Genoa, as confirmed by the mean MSLP map (not shown for brevity).
c) The deepening of the trough is related to the formation, and the transport toward the Mediterranean, of a low/middle-level cold air mass (Figs. 5c,e), which anyway remains quite far from the Tyrrhenian coast, that is still affected by a warm anomaly.
d) This colder air is advected toward the western Mediterranean Basin by higher-than-average surface winds (Figs. 5d-e). This configuration is also typical for the area, associated with Atlantic perturbations that penetrate the Mediterranean Basin through the Rhone Valley / Gulf of Lion. Figure 5e shows an area of stronger-than-average 10m wind just over this area, with mean values of about 10 m s^{-1} for the selected tornadoes cases. Central Italy, Lazio in particular, is hit by southwesterly currents carrying warmer and more humid air toward the Tyrrhenian coast.
Some of these maps show similarities with the results of Bagaglini et al. (2021), although they considered a dataset limited to 20 years and used different procedures.
Figure 6 shows the mean CAPE and DLS values for the 72 representative cases in the CT regions, in order to evaluate the spatial distribution of these fields. As already stated in section 3.1.1, the mean ERA5 convective fields are greater than the 30-year average (not shown), although not extreme.
Moderate-to-high values of the composite CAPE are noticeable on the whole Tyrrhenian Sea; in particular, a local maximum (values greater than 800 J kg^{-1}) is present just off the Tyrrhenian coast of Lazio. Regarding the composite DLS, the map confirms the occurrence of moderate DLS over central Italy (as already assessed in section 3.1.1) and the presence of higher shear values over the Sicily Channel and the southern Tyrrhenian, with relative maxima on the western coasts, probably due to the friction generated by the land-sea contrast.

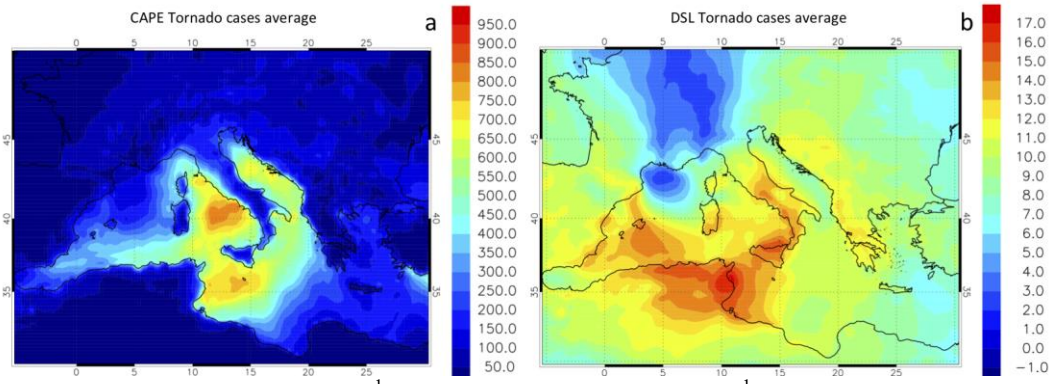

Fig. 6. Convective available potential energy (J kg^{-1}; (a)) and deep layer wind shear (m s^{-1}; (b)) for the 72-tornado cases average.

3.2 The 28 July 2019 case study

In the night between 27 and 28 July 2019, at about 00:25 UTC, an EF2 tornado hit central Lazio, in particular a rural area of the Fiumicino municipality (Fig. 1b). Winds at about 180 km/h and the presence of a mesocyclonic structure were described in the ESWD report.
Born as a waterspout, the vortex became a tornado after landfall, proceeding for about 5 km from WSW towards ENE. It caused widespread damage to homes, cutting down trees and lifting cars; unfortunately, it also caused one casualty. The tornado also passed through a gas station and a part of the runways of the Fiumicino (Rome) airport, fortunately without causing further damages.

3.2.1 Synoptic analysis and instability perspective

The map of sea level pressure and fronts (Fig. 7a; 00:00 UTC on 28-07-2019) reveals the presence of a low-pressure (998 hPa) on the western Mediterranean, resulting from a typical cyclogenesis on the Gulf of Genoa, while a cold front moves toward south-east encountering a positive SST anomaly (Fig. 7b), the highest values being visible in the Ligurian Sea (+4°C). High anomalies (+ 3°C) are also present in the Central Tyrrhenian area, which was crossed by the convective cells (see below).

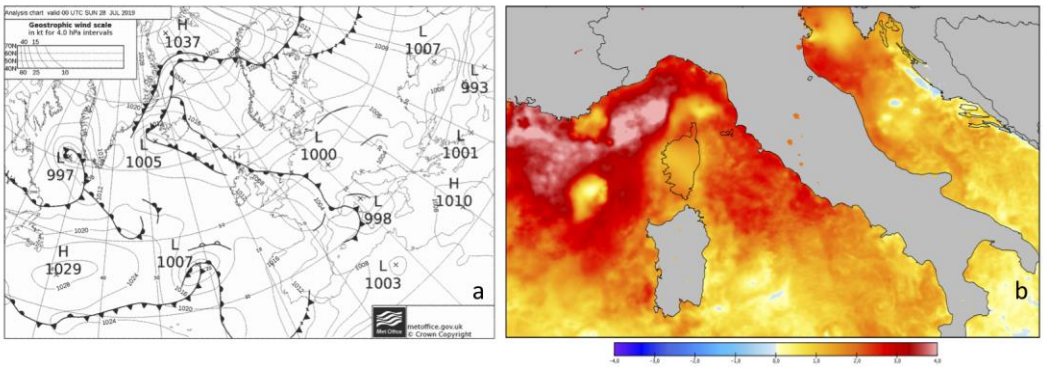

Fig. 7. (a) surface map (sea level pressure [hPa] and weather fronts) at 00:00 UTC, 28-07-2019 (source: metoffice.gov.uk). (b) daily Multi-Scale Ultra High Resolution (MUR) Sea Surface Temperature (SST) anomaly field for the 27-07-2019, computed considering a 2003-2014 climatological mean (JPL Mur MEaSUREs Project, 2015).

The upper-levels maps (Fig. 8, top) at 12 UTC on 27 July and 00 UTC on 28 July, generated from the WRF model simulation (outer domain) show how the synergistic deepening of the diffluent upper-level trough and the low-level cyclogenesis on the Ligurian Sea facilitated the entry of colder air from the NW into the western Mediterranean Basin through the Rhone Valley (Fig. 8, bottom). As a consequence of the eastward evolution of the front, in the lower levels (850 hPa; Fig. 8d) a progressive cooling over central and northwestern Italy is visible. The contrast of air masses near the Tyrrhenian coast is also apparent at 500 hPa, with colder air over the northern Mediterranean and warmer air persisting over southern Italy, associated with an anticyclonic circulation centered over northern Africa.

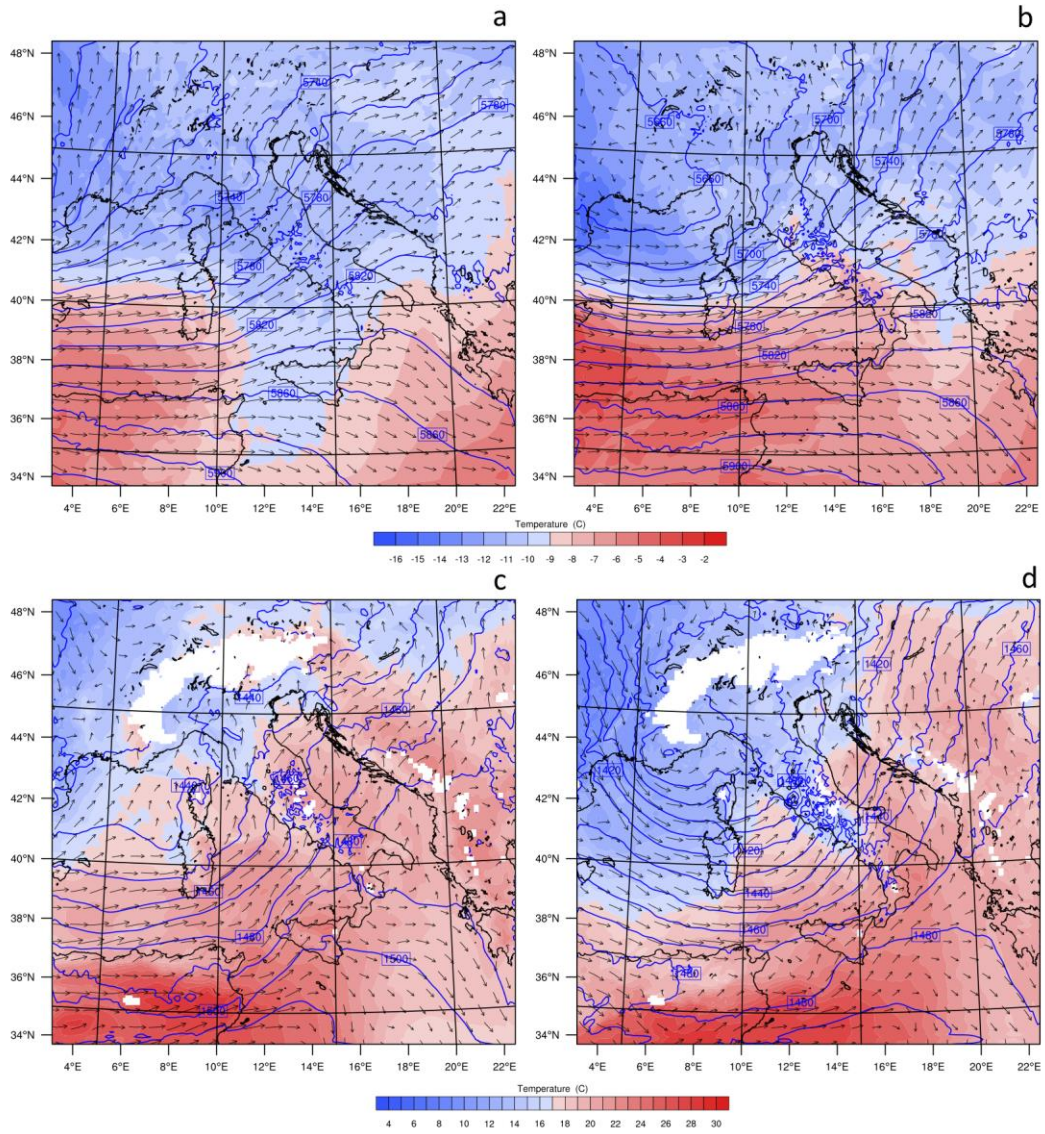

Fig. 8. WRF-outer grid (9 km resolution): temperature (colours, °C), geopotential height (blue-contours, m) and wind vectors at 500 hPa (a,b) and 850 hPa (c,d), on 12:00 UTC, 27-07-2019 (left column) and 00:00 UTC, 28-07-2019 (right column).

Large-scale forcing and mesoscale features contribute to severe convection in the area. A potential vorticity streamer was clearly visible over the western Mediterranean (Fig. 9a), associated to a jet stream developed on the southern flank of the trough. This upper-level PV anomaly, and the related conditions of baroclinic instability, may enhance the cyclonic circulation at the surface, favoring air–sea interaction (Homar et al., 2003; Federico et al., 2007). In the same region, a maximum of MUCAPE is clearly visible (Fig. 9b; values greater than 3000 J kg^{-1}), mostly due to strong equivalent potential temperature difference (greater than 20 K) between 925 hPa and 500 hPa (Fig. 9c). This tongue of high MUCAPE corresponds well to the location of the cold front.

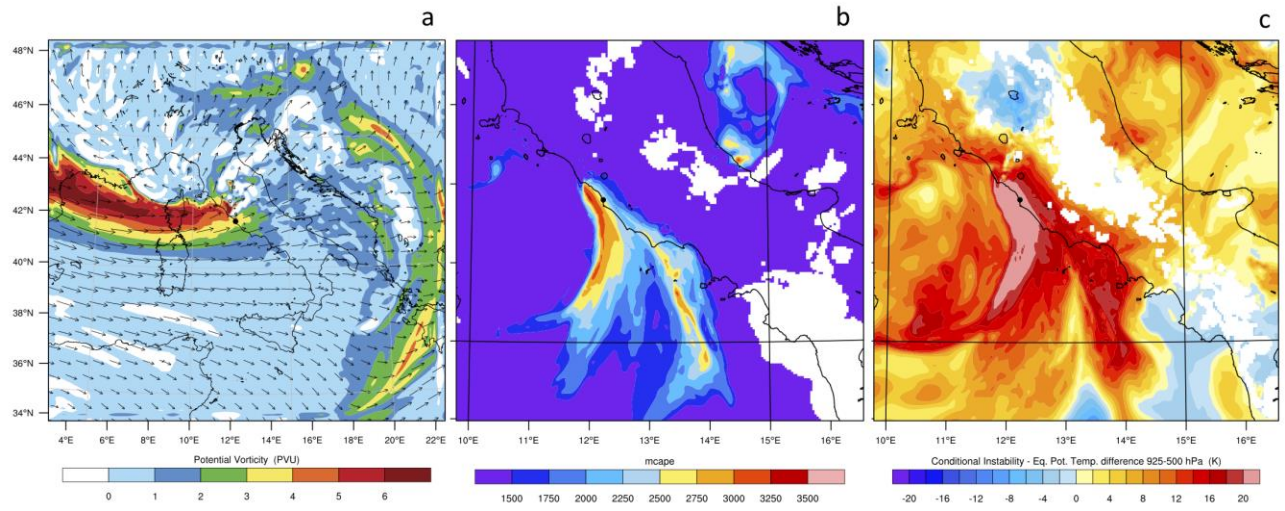

Fig. 9. a) WRF-outer grid (9 km resolution) Potential Vorticity (PV) (colours, PVU) and wind vectors at 300 hPa; b) WRF 3 km grid spacing MUCAPE (J kg^{-1}); c) WRF 3 km grid spacing Equivalent Potential Temperature difference 925-500 hPa (°C). All maps refer to 00:00 UTC, 28-07-2019. The black dot indicates the tornado location.

3.2.2 Mesoscale analysis

In order to analyze the pre-convective environmental characteristics, the soundings / pseudo-soundings in Pratica di Mare at 12 UTC on 27 July are here considered. The comparison of RAOB and WRF model outputs shown in Fig. 10 reveal that the model is able to reproduce accurately the wind and temperature profiles. Vertical wind shear is present in the lower atmospheric layers (below 2000 m), due to weak southeasterlies winds near the surface that rotate from southwest and intensify with height. The temperature profiles show saturation at about 900 hPa and an inversion layer at about 800 hPa (at 850 hPa in WRF model output). This configuration is typical of "loaded-gun" soundings, where the instability can be suddenly released when the uplift is sufficient to remove the convective inhibition. At this time the simulated MUCAPE is high (1740 J kg^{-1}), but even higher in the observations (2130 J kg^{-1}).

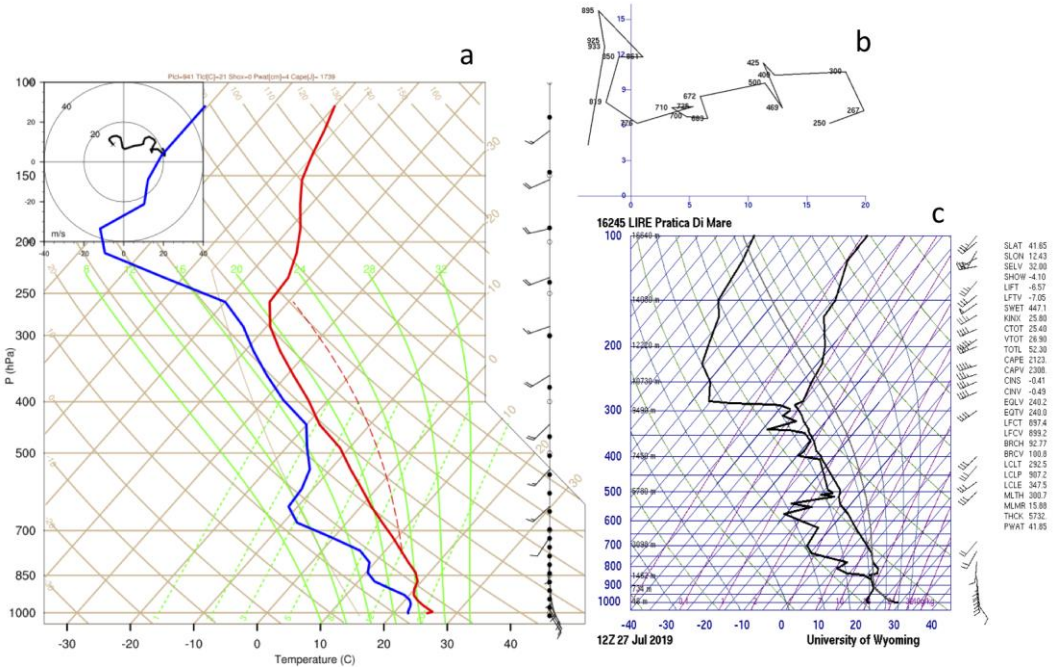

Fig. 10. Skew-T diagrams and hodographs at Pratica di Mare from 1 km grid spacing WRF CTL run (a) and from RAOB sounding (b,c); the maps refer to 12:00 UTC, 27-07-2019. (RAOB data Source: Department of Atmospheric Science, University of Wyoming).

The observed and simulated hodographs are also in good agreement, showing a clockwise low-level curvature that indicates conditions favorable to supercells development (Weisman and Klemp, 1984; 1986). At upper levels the shear appears nearly unidirectional, similar to that found for the 30-years composite analysis (section 3.1.1) and more favorable to the development of multicell convective systems (Chisholm and Renick, 1972).

Figure 11 represents a multi-panel of observed and simulated fields between 00 and 01 UTC, every 30 minutes, around the time of tornado occurrence. The first row shows the strokes number at 00 and 01 UTC. A cluster of strokes is visible just over the area of the tornado, moving eastward; its spatial distribution can be superimposed to the observed maximum values of the composite reflectivity (second row), suggesting that lightning flashes provide good information on the spatio-temporal identification of tornado-spawning cells (Avolio and Miglietta, 2021). The maximum reflectivity simulated in the inner grid of the CTL run (third row) is consistent with the observed patterns (second row). The values of vertical wind speed at 700 hPa (fourth row) and Updraft Helicity (UH) (fifth row) are shown to represent the intensity of the supercells; the usefulness of UH in representing mid-level mesocyclonic rotation is known, using a typical threshold of UH = 50 $m^2 s^{-2}$ (Clark et al., 2012).

The sequence of the UH maps shows the eastward motion of a few scattered cells crossing the Lazio region, with values greater than 300 $m^2 s^{-2}$, especially in northern and southern ends of the convective line; the highest values are simulated few km north of Fiumicino. Similarly, the maps of vertical wind component at 700 hPa reveal a linear pattern of upward motion, crossing the tornado location and the areas north of it. The shape of the system, and the radar reflectivity maps (Figs. 11c-e; the 'yellowish-orange-red' structure in particular), suggest that the tornado may have been caused by a Quasi-Linear Convective System (QLCS) (Weisman and Davis, 1998), i.e. a linearly-oriented zone of high convection (thunderstorms). QLCSs are occasionally associated to tornadoes, which generally tend to be weaker than those generated by isolated supercell thunderstorms (e.g. Trapp et al., 2005).

A QLCS is a type of mesoscale convective system that generally moves in east-west direction parallel to a cold front and, in its evolution, can sometimes form a bowing segment (bow echo). The main ingredients for the formation of these storms are the presence of moisture, lift and instability

conditions; a cold front, which separates cooler air from warm and moist air, is also typical. Convergence in the lower levels can enhance its potential. The thermodynamic large-scale conditions favorable for the genesis of this type of multicell systems are moist southerly flows at low levels, and drier westerly / southwesterly flows aloft, with the storm moving along the mid-tropospheric wind (Wallace and Hobbs, 2006).

All the ingredients mentioned above are found in our case study. In particular, Figure 11 shows that the linear convective system is located ahead of the previously identified cold front (section 3.2.1; figs 7a and 8) and crosses the tornado location few minutes before 00:30 UTC, in good agreement with the tornado report. The 950 hPa convergence/divergence fields and the wind vectors at 00:30 UTC (Fig. 12) show a strong low-level convergence, with southerly winds near the surface on the southern side of the convergence line and westerlies on the western side; to this situation corresponds, at the upper-level, divergence and southwesterly winds (not shown). Observing the motion of the linear structure (Fig. 11) and considering the WRF horizontal winds at various levels (figs. 8, 9), the steering flow for the system is represented by the westerlies / southwesterly upper tropospheric wind.

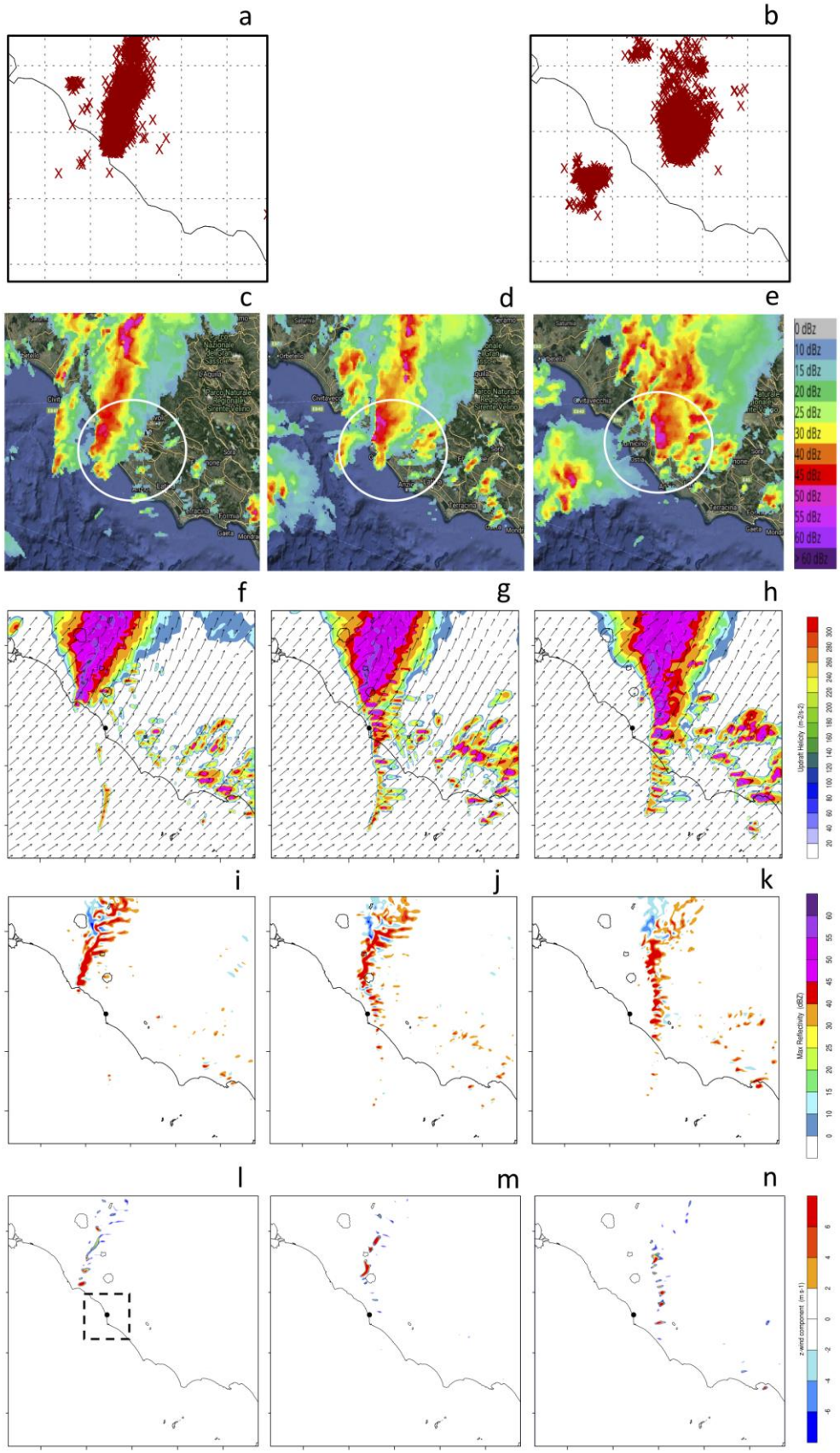

Fig. 11. Lightning activity (cloud-to-ground and intra-cloud data recorded by the LINET network; Betz et al., 2009. The electric discharges are grouped within a 10 km radius and the maps shows the sum of the strokes over 10 min) at 00:00 (a) and 01:00 UTC (b); composite radar reflectivity (dBZ; second row. Data from the automatic system "Dewetra" of the Italian Department of Civil Protection, www.mydewetra.org); WRF maximum reflectivity (dBZ; third row); WRF vertical velocity at 700 hPa (m s^{-1}; fourth row); WRF

Updraft Helicity ($m^2 s^{-2}$; fifth row). All WRF maps refer to the CTL configuration (1 km grid spacing) at 00:00 (first column), 00:30 (second column) and 01:00 (third column) UTC. In the lower left panel, a black dotted square identifies a 40x40 km box around the tornado location (black dot).

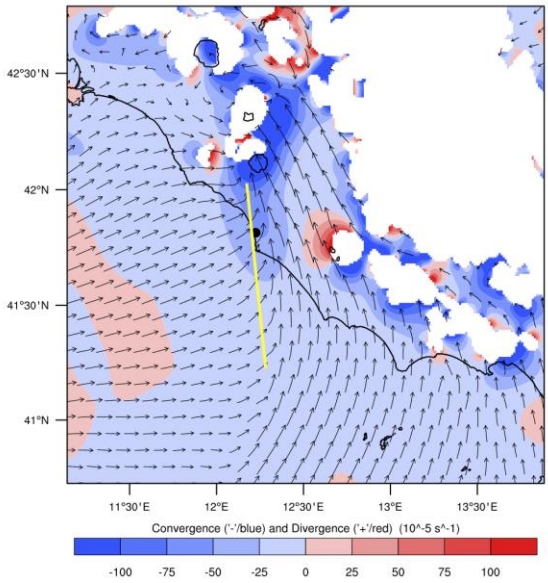

Fig. 12. 950 hPa divergence (positive values; red) / convergence (negative values; blue) (10^{-5} s^{-1}) fields and wind vectors at 00:30 UTC, 28-07-2019. The black dot indicates the tornado location; the yellow line identifies the convergence line.

3.2.3 Sensitivity tests and qualitative model performance evaluation

Some sensitivity tests were also performed to evaluate the role of the SST, the orography, and the surface fluxes in the evolution of this event. For this purpose, we identified a box around the tornado location and calculated the maximum value of some meteorological fields and instability parameters in a time-interval centered at the time of tornado occurrence. Such an approach was adopted in the recent past. For example, Avolio and Miglietta (2021) evaluated the maximum of some instability indices for four tornadoes affecting southern Italy; Grieser and Haines (2020) proposed a tornado risk climatology over Europe, based on the maximum daily values of CAPE, DLS, and significant tornado parameter (STP) in grid cells of 0.5° x 0.5°; Chernokulsky et al. (2020) calculated the maxima of several thermodynamic and kinematic variables within a 100-km area around the location of some observed tornadoes (in the Ural Region) in a 6 h interval.
Here, we consider a small box of 40x40 km (see the black dotted square in the lower-left panel in Fig. 11), and model outputs every 30 minutes from 23:00 to 02:00 UTC.
Having already ascertained the importance of the SST in tornadic supercells in the southeastern Italian regions (Miglietta et al., 2017b; Avolio and Miglietta 2021), we performed three tests aimed at evaluating, also for the present case, the role played by the SST. In particular, in the "MUR_SST" run the initial SST field in the CTL run (taken from the ECMWF-IFS analysis) was replaced by the observed high-resolution (1 km) MUR SST (see Section 3.2.1); in the "SST+1" ("SST-1") run the initial SST values were increased (decreased) uniformly all over the domain by 1 K with respect to the CTL run.
The role of the orography was analyzed in the "HALFTOPO" run, performed by halving the height of the terrain in all the WRF model domains; lastly, the role of sensible and latent heat fluxes was investigated by turning-off the surface fluxes from 18:00 UTC onward ("NOFLUX" run).
Fig. 13 shows the time series of the maximum simulated values of UH (a), vertical wind speed at 700 hPa (W700) (b), SRH03 (c), DLS (d), maximum reflectivity (MAX DBZ) (e), and SCP (f) (see

Table A1) in the 40 x 40 km box for the CTL (black solid lines), MUR_SST (black dotted line), SST+1 (red), SST-1 (blue), NOFLUX (yellow), and HALFTOPO (grey) tests, during the selected time interval (outputs every 30 minutes).

For the CTL run, the maximum values are simulated around the time of tornado occurrence, at about 00:30 UTC, confirming that the simulation is able to reproduce the most favorable conditions for intense convection at the right time. The run "MUR_SST" exhibits a similar evolution, but with slightly higher values for most of the instability parameters. The run SST+1 produces an intensification of the updraft rotation in the supercell as well as greater vertical velocity and higher values for most of the instability parameters, and an anticipation in the evolution of the system (the opposite is observed for the run SST-1). In fact, higher SST implies a warmer and moister lower troposphere, thus more unstable conditions and potentially stronger updrafts are expected.

The maximum CAPE in the CTL run exhibits extreme values (> 3000 J kg^{-1}), as seen in section 3.2.1; also, DLS and SRH03 values appear much higher than average (DLS ≈38 m s^{-1}, SRH ≈600 m^2 s^{-2}). Other instability parameters show very high values at the time of tornado, confirming the favorable conditions of the environment to the supercell development (EHI=8.2; KI=46.4 K; WMAXSHEAR=2330 m^2 s^{-2}; SCP=26; STP=4). Also, updraft rotation appears moderate-to-high (UH=260 m^2 s^{-2}; W700=15 m s^{-1}). The values of the instability parameters are much higher than for a QLCS-related tornado in Spain (Bech et al., 2015), but, compared to the Ionian Italian tornadoes (Avolio and Miglietta, 2021), generated by isolated supercells, the values appear generally smaller, mainly due to the high low-level wind shear present in these cases.

The HALFTOPO run shows lower values for all parameters compared to CTL (Fig. 13); in particular, the halved orography produced a drastic decrease in the DLS and the SRH03, and, consequently, in UH and W700. However, moderate values of maximum reflectivity still appear and the structure of the convective system (Fig. C1; Appendix C) is only slightly modified, with a shift of the orographic triggering northward, closer to the Apennines.

Turning-off the surface heat fluxes leads to a strong inhibition of convective activity (in figure 13 the NOFLUX curves are the lowest). Regarding the structure of the storm, Figure C1 shows that the suppression of the fluxes causes the lost of the linear structure of the convective system, which appears scattered and weaker, especially on its southern side.

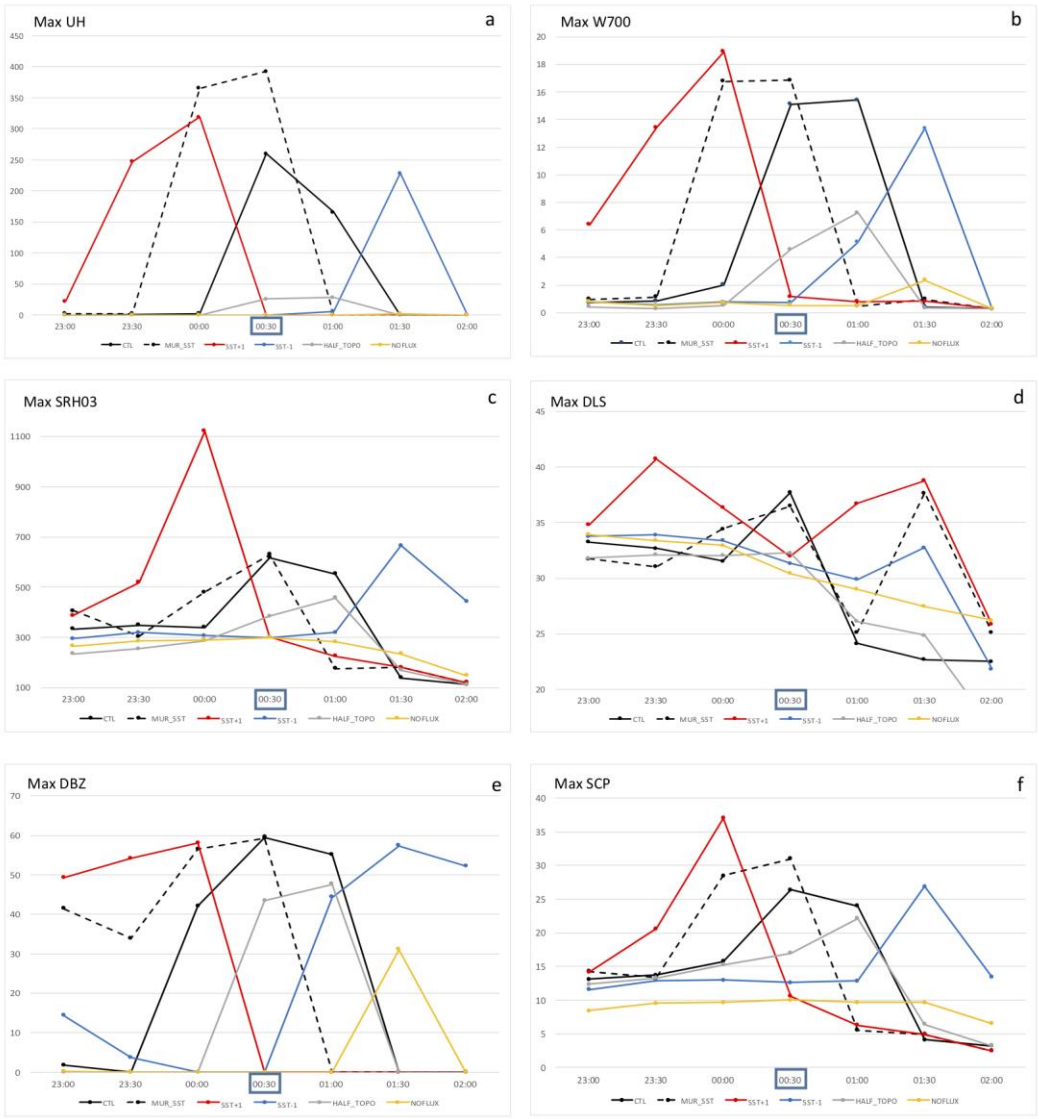

Fig. 13. Time series of the maximum simulated values of UH ($m^2 s^{-2}$; (a)), vertical wind speed at 700 hPa ($m s^{-1}$; (b)), SRH03 ($m^2 s^{-2}$; (c)), DLS ($m s^{-1}$; (d)), maximum composite reflectivity (MAX DBZ) (dBZ; (e)) and SCP (f) in the 40x40 km box for the CTL (black solid lines), MUR_SST (black dotted line), SST+1 (red), SST-1 (blue), NOFLUX (yellow), and HALFTOPO (grey) tests, during the selected time interval reported on the x-axis.

Lastly, further considering the modification of the trajectories and the structure of the tornado spawning cells as the SST varies, figure C2 (Appendix C) shows how the SST+1 (SST-1) run anticipates (delays) the crossing of the convective line over the tornado location (see also Fig. 13), in agreement with Avolio and Miglietta (2021), where the authors hypothesized that the acceleration can be attributed to the DMM (downward momentum mixing) mechanism (Hayes et al., 1989).

4. Summary and Conclusions

The present work focuses on the study of tornado events on one of the Italian hotspots for such extreme weather episodes, the central Tyrrhenian regions of the peninsula. Starting from the climatology of the significant tornadoes based on the 1990-2021 years, a synoptic/mesoscale analysis, performed through the use of both radiosonde observations and ERA5 reanalysis, permits

to identify the main synoptic patterns and the main mesoscale characteristics associated with these events.

93 tornadoes were identified in the area and in the considered period. A pronounced upper-level trough over the central Mediterranean Sea and a low-pressure over northwestern Italy dominate the mean synoptic conditions associated with the occurrence of these tornadoes, thus the tornado-spawning cells generally reach the central Tyrrhenian coast pushed by southwesterly winds. During these events, higher-than-average surface winds entered the western Mediterranean through the Rhône Valley / Gulf of Lion, the favored gateway of the Atlantic perturbations for the Mediterranean basin. The mean values of some instability parameters are moderate-to-high, with CAPE of about 700 J kg^{-1} and deep layer wind shear of about 15 m s^{-1}. The analysis of the mean wind profiles, performed at a representative sounding site, suggests an environment favorable to the development of multicell systems.

A specific tornado case study is also analyzed in this work, concerning a significant event (EF2) that hit the central Tyrrhenian coast on 28 July 2019. The WRF model satisfactory simulates conditions favorable to severe convection and the presence of a linear convective system that triggered the tornado. This is the first time that such a triggering mechanism is identified for a tornado in Italy.

The model simulates very high values for the instability parameters/indices usually employed to diagnose the possibility of severe convection. Specific sensitivity tests confirm the important role of the SST in the tornado development, while the orography determines the area where convection was triggered; thus, their accurate representation permits to reproduce properly the structure of the convective system.

The satisfactory simulation of the EF2 tornado studied in the present paper confirms the potential benefit of an opportunely tuned mesoscale numerical modeling system, hopefully integrated with advanced observational tools, both for the identification of the environmental conditions that favor severe convection and for the development of a warning system dedicated to the prediction of such severe events (Miglietta and Rotunno, 2016). This is a relevant issue due to the high impact of these phenomena, which will be further exacerbated as a consequence of the climate change (e.g., Seeley and Romps, 2015; Púcˇik et al., 2017).

Acknowledgments

The Italian Department of Civil Protection is acknowledged for the radar images (derived by the automatic system Dewetra). LINET data were granted by Nowcast GmbH, within a scientific agreement between H.-D. Betz and the Satellite Meteorological Group of CNR-ISAC in Rome. The authors would like to tank Prof. Joan Bech for some useful suggestions.

Funding: *This research did not receive any specific grant from funding agencies in the public, commercial, or not-for-profit sectors.*

Figure captions

Fig. 1. The main locations cited in the text. On the right: 1 km grid spacing WRF model inner domain and terrain height (m).

Fig. 2. Position of the 93 tornadoes during the 30-years period in the CT regions; the different colors refer to the different seasons.

Fig. 3. Composite Skew-T diagrams and hodographs at Pratica di Mare from RAOB sounding (a,c) and from ERA5 reanalysis (b,d). (RAOB data Source: Department of Atmospheric Science, University of Wyoming).

Fig. 4. Boxplots for CAPE (a), KI (b), TT (c), DLS (d), WMAXSHEAR (e) and SRH03 (f), for both ERA5 (box on the left) and RAOB (box on the right) data, related to the 63 selected proximity soundings. The 25th, the 50th (median) and the 75th percentiles are shown, as well as the extremes. Mean values are also reported on x-axis.

Fig. 5. Anomalies of the ERA5 fields of geopotential height at 500 hPa (m; (a)), mean sea level pressure (hPa; (b)), temperature at 850 hPa (K; (c)). Anomalies are calculated considering the mean values of the selected 72 tornado cases with respect to a 30-year period average (1990–2021). The 10-m wind (vector and speed; m/s) are reported for the 30-years average (d) and for the 72-tornado cases average (e). *(For interpretation of the references to colour in this figure legend, and all the others in the manuscript, the reader is referred to the web version of this article).*

Fig. 6. Convective available potential energy (J kg^{-1}; (a)) and deep layer wind shear (m s^{-1}; (b)) for the 72-tornado cases average.

Fig. 7. (a) surface map (sea level pressure [hPa] and weather fronts) at 00:00 UTC, 28-07-2019 (source: metoffice.gov.uk). (b) daily Multi-Scale Ultra High Resolution (MUR) Sea Surface Temperature (SST) anomaly field for the 27-07-2019, computed considering a 2003-2014 climatological mean (JPL Mur MEaSUREs Project, 2015).

Fig. 8. WRF-outer grid (9 km resolution): temperature (colours, °C), geopotential height (blue-contours, m) and wind vectors at 500 hPa (a,b) and 850 hPa (c,d), on 12:00 UTC, 27-07-2019 (left column) and 00:00 UTC, 28-07-2019 (right column).

Fig. 9. a) WRF-outer grid (9 km resolution) Potential Vorticity (PV) (colours, PVU) and wind vectors at 300 hPa; b) WRF 3 km grid spacing MUCAPE (J kg^{-1}); c) WRF 3 km grid spacing Equivalent Potential Temperature difference 925-500 hPa (°C). All maps refer to 00:00 UTC, 28-07-2019. The black dot indicates the tornado location.

Fig. 10. Skew-T diagrams and hodographs at Pratica di Mare from 1 km grid spacing WRF CTL run (a) and from RAOB sounding (b,c); the maps refer to 12:00 UTC, 27-07-2019. (RAOB data Source: Department of Atmospheric Science, University of Wyoming).

Fig. 11. Lightning activity (cloud-to-ground and intra-cloud data recorded by the LINET network; Betz et al., 2009. The electric discharges are grouped within a 10 km radius and the maps shows the sum of the strokes over 10 min) at 00:00 (a) and 01:00 UTC (b); composite radar reflectivity (dBZ; second row. Data from the automatic system "Dewetra" of the Italian Department of Civil Protection, www.mydewetra.org); WRF maximum reflectivity (dBZ; third row); WRF vertical velocity at 700 hPa (m s^{-1}; fourth row); WRF Updraft Helicity (m^2 s^{-2}; fifth row). All WRF maps refer to the CTL configuration (1 km grid spacing) at 00:00 (first column), 00:30 (second column) and 01:00 (third column) UTC. In the lower left panel, a black dotted square identifies a 40x40 km box around the tornado location (black dot).

Fig. 12. 950 hPa divergence (positive values; red) / convergence (negative values; blue) (10^{-5} s^{-1}) fields and wind vectors at 00:30 UTC, 28-07-2019. The black dot indicates the tornado location; the yellow line identifies the convergence line.

Fig. 13. Time series of the maximum simulated values of UH (m^2 s^{-2}; (a)), vertical wind speed at 700 hPa (m s^{-1}; (b)), SRH03 (m^2 s^{-2}; (c)), DLS (m s^{-1}; (d)), maximum composite reflectivity (MAX DBZ) (dBZ; (e)) and SCP (f) in the 40x40 km box for the CTL (black solid lines), MUR_SST (black dotted line), SST+1 (red), SST-1 (blue), NOFLUX (yellow), and HALFTOPO (grey) tests, during the selected time interval reported on the x-axis.

Fig. B1 Position of the 445 tornadoes during the 30-years period in Italy; the different colors refer to the different seasons.

Fig. C1 WRF maximum reflectivity (dBZ; first row); WRF vertical velocity at 700 hPa (m s^{-1}; second row); WRF Updraft Helicity (m^2 s^{-2}; third row), for the HALFTOPO (first column) and NOFLUX (second column) tests. All maps refer to the 00:30 UTC, 28-07-2019. The black dot indicates the tornado location.

Fig. C2 WRF Updraft Helicity (m^2 s^{-2}; third row), for the SST-1 (left), CTL (center) and SST+1 (right) tests. All maps refer to the 00:30 UTC, 28-07-2019.

APPENDIX A

In this Appendix, the equations for some calculated parameters considered in the manuscript are shown (Table A1).

Parameter Equation	Long Name	Units	References
DLS = $\lvert \mathbf{v}_{500}\text{-}\mathbf{v}_{1000} \rvert$	*Deep Layer Shear*	m s^{-1}	*Weisman and Klemp (1982)*
SRH03 = $-\int_{1000}^{700} \mathbf{k} \cdot \left[(\mathbf{v}-\mathbf{c}) \times \frac{\partial \mathbf{v}}{\partial \mathbf{z}}\right] \mathbf{dz}$	*Storm Relative Helicity (0-3 km)*	m^2 s^{-2}	*Davies-Jones et al. (1990)*
WMAXSHEAR = $\sqrt{2 \cdot \mathbf{CAPE}} \cdot \mathbf{DSL}$	-	m^2 s^{-2}	*Taszarek et al. (2017)*
UH = $\int_{2\ \mathbf{km}}^{5\ \mathbf{km}} (\mathbf{v} \cdot \mathbf{k}) \cdot \boldsymbol{\zeta}\, \mathbf{dz}$	*Updraft Helicity*	m^2 s^{-2}	*Kain et al. (2008)*
KI = $(T_{850}\text{-}T_{500}) + Td_{850}\text{-}(T_{700}\text{-}Td_{700})$	*K index*	K	*George (1960)*
TT = $(T_{850}\text{-}T_{500}) + (Td_{850}\text{-}T_{500})$	*Total Totals index*	K	*Miller (1972)*
SCP = (CAPE / 1000) • (SRH03 / 50) • (DLS / 20)	*Supercell Composite Parameter*	-	*Thompson et al. (2004, 2012) (modified formulation)*
STP = (sbCAPE / 1500) • (2000-sbLCL) / 1000) • (SRH01 / 150) • (DLS/20)	*Significant Tornado Parameter*	-	*Thompson et al. (2004, 2012) (modified formulation)*
EHI = (CAPE • SRH03) / (160000)	*Energy Helicity Index*	-	*Davies and Johns (1993)*

Table A1. Equations, units and references for the calculated parameters. v is the horizontal wind vector (the numbers, when no units appear, refer to the vertical pressure level); k is the upward unit vector; c is the storm motion vector; ζ is the vertical component of vorticity; T is the temperature; Td is the dew point temperature; CAPE is the Convective Available Potential Energy; LCL is the Lifted Condensation Level; the prefix "sb" means "Surface Based".

APPENDIX B

In this Appendix, the figure B1 shows the positions of the 445 tornadoes during the 30-years period; the different colors refer to the different seasons. This update climatology of EF1+ tornadoes confirms that the Italian most affected areas by tornadoes are: The Po Valley, the Central Italy Tyrrhenian coasts (CT in the following) (Lazio in particular) and the South-Eastern Italy (SE in the following) (Apulia in particular) (see Fig. 1 for the locations).
About the 80% of EF1+ tornadoes in Italy occur, more or less equally, during the summer (178 events) and the autumn (174 events).

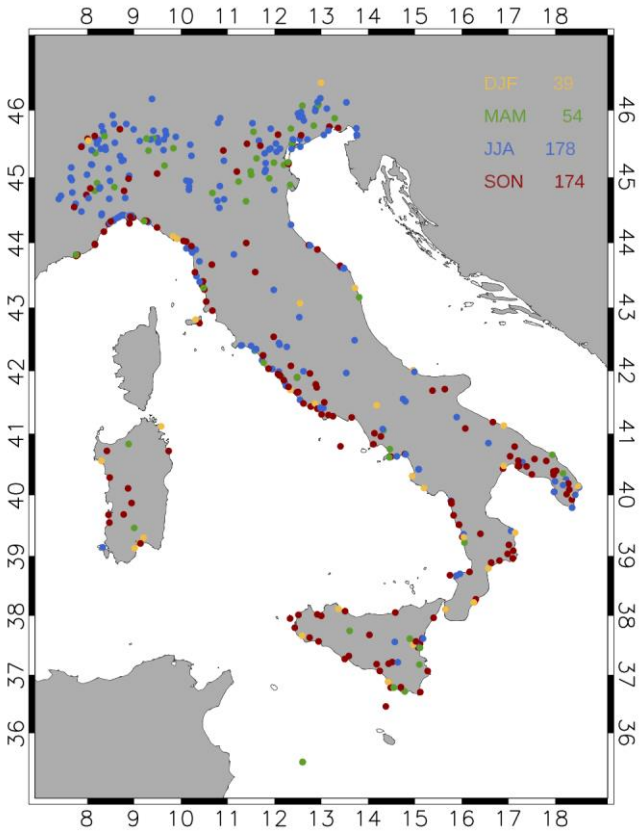

Fig. B1 Position of the 445 tornadoes during the 30-years period in Italy; the different colors refer to the different seasons.

APPENDIX C

In this Appendix, a graphical – qualitative comparison between the sensitivity runs SST-1, SST+1, HALFTOPO and NOFLUX, discussed in section 3.2.3.1, are reported.
In figure C1 are reported the MAX_DBZ (first row), W700 (second row) and UH (third row) fields, valid at the 00:30 UTC, for the HALFTOPO and NOFLUX tests.
In figure C2 is reported the UH, valid at the 00:30 UTC, for the SST-1, CTL and SST+1 tests.

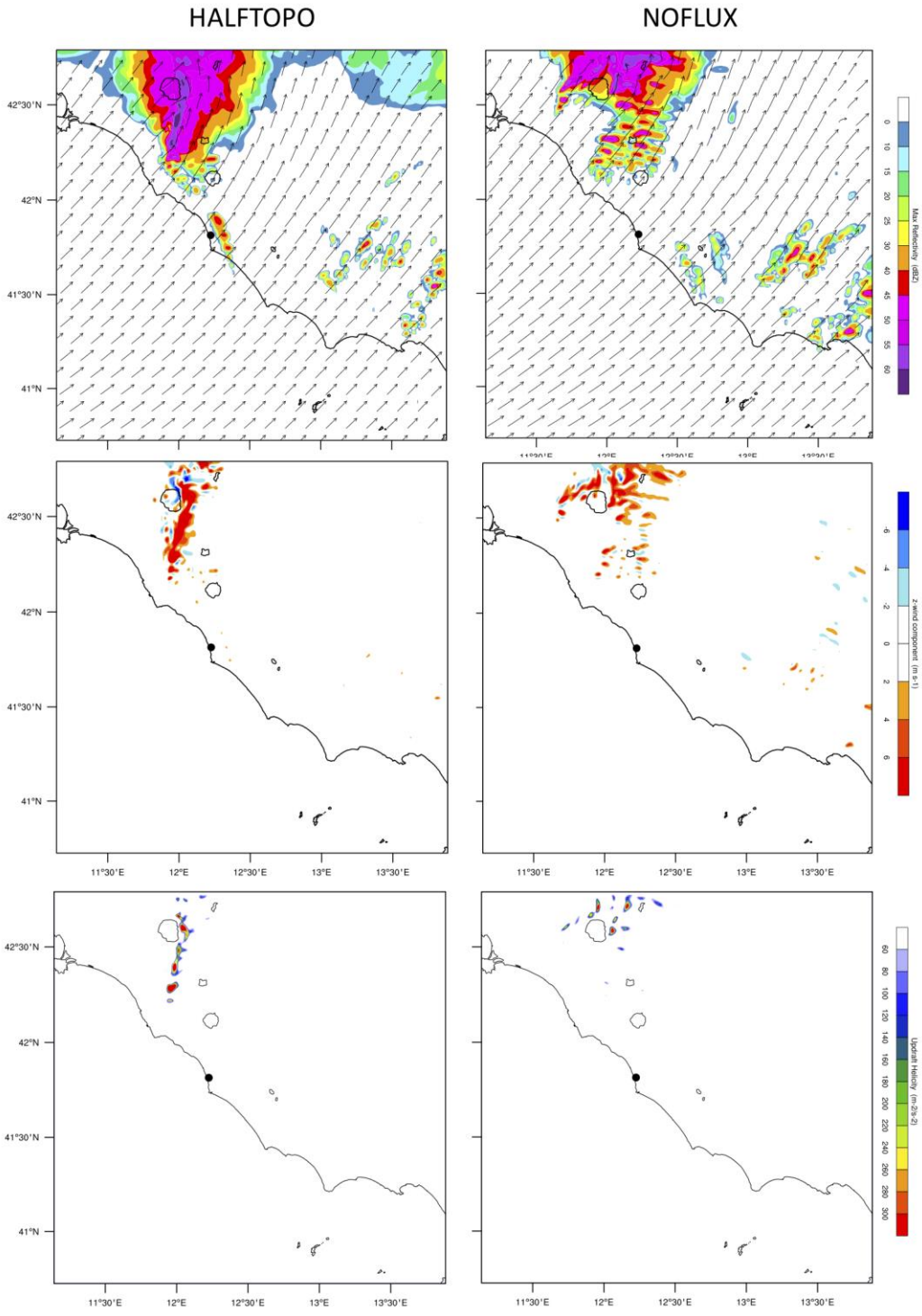

Fig. C1 WRF maximum reflectivity (dBZ; first row); WRF vertical velocity at 700 hPa (m s^{-1}; second row); WRF Updraft Helicity (m^2 s^{-2}; third row), for the HALFTOPO (first column) and NOFLUX (second column) tests. All maps refer to the 00:30 UTC, 28-07-2019. The black dot indicates the tornado location.

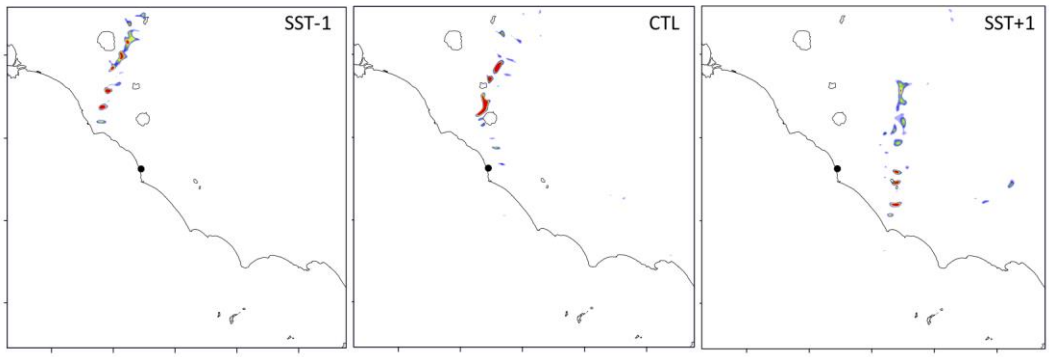

Fig. C2 WRF Updraft Helicity ($m^2 s^{-2}$; third row), for the SST-1 (left), CTL (center) and SST+1 (right) tests. All maps refer to the 00:30 UTC, 28-07-2019.

References

Antonescu, B., Schultz, D.M., Lomas, F., Kühne, T., 2016. Tornadoes in Europe: synthesis of the observational datasets. Mon. Weather Rev. 144, 2445–2480. https://doi.org/ 10.1175/MWR-D-15-0298.1.

Antonescu, B., Schultz, D.M., Holzer, A., Groenemeijer, P., 2017. Tornadoes in Europe: an underestimated threat. Bull. Am. Meteorol. Soc. 98, 713–728. https://doi.org/ 10.1175/BAMS-D-16-0171.1.

Aran, M., Amaro, J., Arús, J., Bech, J., Figuerola, F., Gaya`, M., Vilaclara, E., 2009. Synoptic and mesoscale diagnosis of a tornado event in Castellcir, Catalonia, on 18th October 2006. Atmos. Res. 93 (1–3), 147–160. https://doi.org/10.1016/j. atmosres.2008.09.031.

Ashley, W. S., A. M. Haberlie, and J. Strohm, 2019. A climatology of quasi-linear convective systems and their hazards in the United States. Wea. Forecasting, 34, 1605–1631. https://doi.org/10.1175/ WAF-D-19-0014.1.

Avolio, E., Nisi, L., Panziera, L., Peyraud, L., Miglietta, M.M., 2020. A multi-sensor and modeling analysis of a severe convective storm in Lake Maggiore area (northwestern Italy). Atmos. Res. 242, 105008. https://doi.org/10.1016/j.atmosres.2020.105008.

Avolio E. and Miglietta M.M., 2021. Multiple tornadoes in the Italian Ionian regions: Observations, sensitivity tests and mesoscale analysis of convective storm environmental parameters. Atmos. Res. 263, 105800. https://doi.org/10.1016/j.atmosres.2021.105800.

Bagaglini, L., Ingrosso, R., Miglietta, M.M., 2021. Synoptic patterns and mesoscale precursors of Italian tornadoes. Atmos. Res. 253, 105503. https://doi.org/10.1016/j. atmosres.2021.105503.

Bech, J., Pineda, N., Rigo, T., Aran, M., Amaro, J., Gaya`, M., Arús, J., Montanya`, J., van der Velde, O., 2011. A Mediterranean nocturnal heavy rainfall and tornadic event. Part I: Overview, damage survey and radar analysis. Atmos. Res. 100 (4), 621–637. https://doi.org/10.1016/j.atmosres.2010.12.024.

Bech, J., Arús, J., Cast´an, S., Pineda, N., Rigo, T., Montanya`, J., van der Velde, O., 2015. A study of the 21 March 2012 tornadic quasi linear convective system in Catalonia. Atmos. Res. 158–159, 192–209. https://doi.org/10.1016/j.atmosres.2014.08.009.

Betz, H.-D., Schmidt, K., Laroche, P., Blanchet, P., Oettinger, P., Defer, E., Dziewit, Z., Konarski, J., 2009. LINET-an international lightning detection network in Europe. Atmos. Res. 91, 564–573.

Brooks, H.E., Lee, J.W., Craven, J.P., 2003. The spatial distribution of severe thunderstorm and tornado environments from global reanalysis data. Atmos. Res. 67–68, 73–94. https://doi.org/10.1016/S0169-8095(03)00045-0.

Buckingham, T. J., & Schultz, D. M., 2020. Synoptic-Scale Environments and Precipitation Morphologies of Tornado Outbreaks from Quasi-Linear Convective Systems in the United Kingdom, Weather and Forecasting, 35(5), 1733-1759.

Chernokulsky, A., Shikhov, A., Bykov, A., Azhigov, I., 2020. Satellite-based study and numerical forecasting of two Tornado outbreaks in the Ural region in June 2017. Atmosphere 11, 1146. https://doi.org/10.3390/atmos11111146.

Chisholm, A. J., and J. H. Renick, 1972. The kinematics of multi-cell and supercell Alberta hailstorms. Research Council of Alberta Hail Studies Report **72-2**, 24–31.

Clark, A.J., Kain, J.S., Marsh, P.T., Correia Jr., J., Xue, M., Kong, F., 2012. Forecasting tornado pathlengths using a three-dimensional object identification algorithm applied to convection-allowing forecasts. Wea. Forecast. 27, 1090–1113.

Clark, M.R. 2013: A provisional climatology of cool-season convective lines in the UK. Atmos. Res., 123, 180–196, https://doi.org/ 10.1016/j.atmosres.2012.09.018.

Corfidi, S.F., Meritt, J.H. and Fritsch, J.M., 1996. Predicting the movement of mesoscale convective complexes. *Weather and Forecasting*, **11**, 41 46.

Corfidi, S.F., 2003. Cold pools and MCS propagation: forecasting the motion of downwind-developing MCSs. Wea. Forecasting 18, 997–1017.

Craven, J.P., Brooks, H.E., 2004. Baseline climatology of sounding derived parameters associated with deep moist convection. Natl. Weather Dig. 28, 13–24.

Davies-Jones, R., Burgess, D.W., Foster, M., 1990. Test of helicity as a forecast parameter. In: Preprints, 16th Conf. on Severe Local Storms, Kananaskis Park, AB, Canada, Amer. Meteor. Soc, pp. 588–592.

Davies, J.M., Johns, R.H., 1993. Some wind and instability parameters associated with strong and violent tornadoes: 1. In: Wind Shear and Helicity. American Geophysical Union (AGU), pp. 573–582. https://doi.org/10.1029/GM079p0573.

Doswell C., H. E. Brooks, and N. Dotzek, 2009. On the implementation of the enhanced Fujita scale in the USA. Atmos. Res., 93, 554–563, https://doi.org/10.1016/j.atmosres.2008.11.003.

Dotzek N. 2003. An updated estimate of tornado occurrence in Europe. *Atmos. Res.* **67–68**:153–161.

Dotzek, N., P. Groenemeijer, B. Feuerstein, and A. M. Holzer, 2009. Overview of ESSL's severe convective storms research using the European Severe Weather Database ESWD. Atmos. Res., 93, 575−586

Federico, S., Avolio, E., Bellecci, C., Lavagnini, A., and Walko, R. L., 2007. Predictability of intense rain storms in the Central Mediterraneanbasin: sensitivity to upper-level forcing, Adv. Geosci., 12, 5–18, https://doi.org/10.5194/adgeo-12-5-2007.

Gatzen, C., 2011. A 10-year climatology of cold-season narrow cold-frontal rainbands in Germany. Atmos. Res. 100 (4), 366–370.

Gensini, V. A., and W. S. Ashley, 2011. Climatology of potentially severe convective environments from the North American Regional Reanalysis. Electron. J. Severe Storms Meteor, 6 (8), http:// www.ejssm.org/ojs/index.php/ejssm/article/viewArticle/85.

George, J.J., 1960. Weather Forecasting for Aeronautics. Academic press, pp. 673.

Giaiotti, D.B., Giovannoni, M., Pucillo, A., Stel, F., 2007. The climatology of tornadoes and waterspouts in Italy. Atmos. Res. 83, 534–541.

Gianfreda, F., Miglietta, M.M., Sansò, P., 2005. Tornadoes in southern Apulia (Italy). Nat. Hazards 34, 71–89.

Goliger, A. M., and R. V. Milford, 1998. A review of worldwide occurrence of tornadoes. J. Wind Eng. Ind. Aerodyn., 74–76, 111–121, https://doi.org/10.1016/S0167-6105(98)00009-9.

Grieser, J., Haines, P., 2020. Tornado risk climatology in Europe. Atmosphere 11 (7), 768. https://doi.org/10.3390/atmos11070768.

Groenemeijer, P., van Delden, A., 2007. Sounding-derived parameters associated with large hail and tornadoes in the Netherlands. Atmos. Res. 83, 473–487. https://doi. org/10.1016/j.atmosres.2005.08.006.

Groenemeijer, P., Kühne, T., 2014. A climatology of Tornadoes in Europe: results from the European Severe Weather Database. Mon. Weather Rev. 142, 4775–4790. https://doi.org/10.1175/MWR-D-14-00107.1.

Hayes, S.P., McPhaden, M.J., Wallace, J.M., 1989. The in uence of sea surface temperature on surface wind in the eastern equatorial Paci c. J. Clim. 2, 1500–1506.

Hersbach, H., Bell, B., Berrisford, P., et al., 2020. The ERA5 global Reanalysis. Q. J. R. Meteorol. Soc. 146, 1999–2049. https://doi.org/10.1002/qj.3803.

Homar, V., Gay`a, M., Romero, R., Ramis, S., Alonso, S., 2003. Tornadoes over complex terrain: an analysis of the 28th August 1999 tornadic event in eastern Spain. Atmos. Res. 67–68, 301–317. https://doi.org/10.1016/S0169-8095(03)00064-4.

Hong, S.-Y., Lim, J.-O.J., 2006. The WRF single-moment 6-class microphysics scheme (WSM6). J. Korean Meteorol. Soc. 42, 129–151.

Iacono, M.J., Delamere, J.S., Mlawer, E.J., Shephard, M.W., Clough, S.A., Collins, W.D., 2008. Radiative forcing by long–lived greenhouse gases: calculations with the AER radiative transfer models. J. Geophys. Res. 113, D13103.

Ingrosso, R., Lionello, P., Miglietta, M.M., Salvadori, G., 2020. A statistical investigation of mesoscale precursors of significant tornadoes: the Italian case study. Atmosphere 11, 301. https://doi.org/10.1002/joc.5526.

Janjic, Z.I., 1994. The Step–Mountain Eta Coordinate Model: further developments of the convection, viscous sublayer, and turbulence closure schemes. Mon. Wea. Rev. 122, 927–945. https://doi.org/10.1175/1520-0493(1994)122<0927:TSMECM>2.0.CO; 2.

Jimenez, P.A., Dudhia, J., Gonzàlez-Rouco, J.F., Navarro, J., Montàvez, J.P., García- Bustamante, E., 2012. A revised scheme for the WRF surface layer formulation. Mon. Wea. Rev. 140, 898–918. https://doi.org/10.1175/MWR-D-11-00056.1.

JPL MUR MEaSUREs Project. 2015. GHRSST Level 4 MUR Global Foundation Sea Surface Temperature Analysis (v4.1). Ver. 4.1. PO.DAAC, CA, USA. Dataset accessed [2021-11-04] at https://doi.org/10.5067/GHGMR-4FJ04.

Kain, J.S., et al., 2008. Some practical considerations regarding horizontal resolution in the rst generation of operational convection-allowing NWP. Wea. Forecast. 23, 931–952.

Miglietta, M.M., Rotunno, R., 2016. An EF3 Multivortex Tornado over the Ionian Region: is it time for a dedicated warning system over Italy? Bull. Am. Meteor. Soc. 97, 337–344. https://doi.org/10.1175/BAMS-D-14-00227.1.

Miglietta, M., Mazon, J., Rotunno, R., 2017a. Numerical simulations of a tornadic supercell over the Mediterranean. Weather Forecast. 32, 1209–1226. https://doi. org/10.1175/WAF-D-16-0223.1.

Miglietta, M., Mazon, J., Motola, V., Pasini, A., 2017b. Effect of a positive sea surface temperature anomaly on a Mediterranean tornadic supercell. Sci. Rep. 7 https://doi. org/10.1038/595s41598-017-13170-0.

Miglietta, M.M., Matsangouras, I.T., 2018. An updated climatology of tornadoes and waterspout in Italy. Int. J. Climatol. 1–17. https://doi.org/10.1002/joc.5526.

Miller, R.C., 1972. Notes on analysis and severe storm forecasting procedures of the Air Force Global Weather Center, AWS Tech. Report 200 (Rev.), Headquarters Air Weather Service, Scott AFB. pp. 106.

Mulder, K. J., and D. M. Schultz, 2015. Climatology, storm morphologies, and environments of tornadoes in the British Isles: 1980–2012. Mon. Wea. Rev., 143, 2224–2240, https://doi.org/ 10.1175/MWR-D-14-00299.1.

Palmieri, S., Pulcini, A., 1978. Trombe d'aria sull'Italia. Riv. Meteorol. Aeronaut. 4, 263–277.

Pilguj, N., Taszarek, M., Allen, J. T., & Hoogewind, K. A., 2022. Are trends in convective parameters over the United States and Europe consistent between reanalyses and observations?, *Journal of Climate* (published online ahead of print

2022).

Pleim, J.E., 2007. A combined local and non-local closure model for the atmospheric boundary layer. Part 1: model description and testing. J. Appl. Meteorol. Climatol. 46, 1383–1395.

Púcˇik, T., Groenemeijer, P., Rädler, A.T., Tijssen, L., Nikulin, G., Prein, A.F., van Meijgaard, E., Fealy, R., Jacob, D. and Teichmann, C. (2017) Future changes in European severe convection environments in a regional climate model ensemble. Journal of Climate, 30, 6771–6794. https://doi.org/10.1175/JCLI-D-16-0777.1.

Ramis, C., Arús, J., López, J.M., Mestres, A.M., 1997. Two cases of severe weather in Catalonia (Spain), an observational study. Meteorol. Appl. 4, 207–217.

Rasmussen, E.N., Blanchard, D.O., 1998. A baseline climatology of sounding-derived supercell and tornado forecast parameters. Wea. Forecast. 13, 1148–1164.

Rasmussen, E. N., 2003. Refined supercell and tornado forecast parameters. Wea. Forecasting, 18, 530–535, https://doi.org/ 10.1175/1520-0434(2003)18,530:RSATFP.2.0.CO;2.

Renko, T., Kuzmi´c, J., Sˇoljan, V., Mahovi´c, N.S., 2016. Waterspouts in the Eastern Adriatic from 2001 to 2013. Nat. Hazards 82, 441–470. https://doi.org/10.1007/ s11069-016-2192-5.

Rodriguez, O., Bech, J., 2018. Sounding-derived parameters associated with tornadic storms in Catalonia. Int. J. Climatol. 38, 2400–2414. https://doi.org/10.1002/ joc.5343.

Rodríguez, O., Bech, J., 2020a. Tornadic environments in the Iberian Peninsula and the Balearic Islands based on ERA5 reanalysis. Int. J. Climatol. 41–S1 https://doi.org/10.1002/joc.6825.

Romero, R., Gayà, M. and Doswell, C.A., 2007. European climatology of severe convective storm environmental parameters: a test for significant tornado events. Atmospheric Research, 83 (2–4), 389–404. https://doi.org/10.1016/j.atmosres.2005.06.011.

Rotunno, R. On the Evolution of Thunderstorm Rotation. *Mon. Weather Rev.* **1981**, *109*, 577–586.

Seeley, J.T. and Romps, D.M. (2015) The effect of global warming on severe thunderstorms in the United States. Journal of Climate, 28, 2443–2458. https://doi.org/10.1175/JCLI-D-14-00382.1.

Skamarock, W.C., Klemp, J.B., Dudhia, J., Gill, D.O., Liu, Z., Berner, J., Wang, W., Powers, J.G., Duda, M.G., Barker, D.M., Huang, X.-Y., 2019. A description of the advanced research WRF version 4. In: NCAR Tech. Note NCAR/TN-556+STR, p. 145. https://doi.org/10.5065/1dfh-6p97.

Taszarek, M., Kolendowicz, L., 2013. Sounding-derived parameters associated with tornado occurrence in Poland and universal tornadic index. Atmos. Res. 134, 186–197. https://doi.org/10.1016/j.atmosres.2013.07.016.

Taszarek, M., Brooks, H.E., Czernecki, B., 2017. Sounding-derived parameters associated with convective hazards in Europe. Mon. Weather Rev. 145, 1511–1528. https://doi.org/10.1175/MWR-D-16-0384.1.

Taszarek, M., Allen, J.T., Púˇcik, T., Hoogewind, K.A., Brooks, H.E., 2020. Severe convective storms across Europe and the United States. Part 2: ERA5 environments associated with lightning, large hail, severe wind and tornadoes. J. Climate 1–53. https://doi.org/10.1175/JCLI-D-20-0346.1.

Tessendorf, S.A., Trapp, R.J., 2000. On the climatological distribution of tornadoes within quasi-linear convective systems. Preprints, 20th Conf. on Severe Local Storms, Orlando, FL, Amer. Meteor. Soc, pp. 134–137.

Tewari, M., Chen, F., Wang, W., Dudhia, J., LeMone, M.A., Mitchell, K., Ek, M., Gayno, G., Wegiel, J., Cuenca, R.H., 2004. Implementation and verification of the unified NOAH land surface model in the WRF model. In: 20th Conference on Weather Analysis and Forecasting/16th Conference on Numerical Weather Prediction, pp. 11–15.

Thompson, R.L., Edwards, R., Mead, C.M., 2004. An update to the supercell composite and significant tornado parameters. In: Preprints, 22nd Conf. on Severe Local Storms, Hyannis, MA, P8.1. Amer. Meteor. Soc.. Available online at. https://ams.confex.com/ams/pdfpapers/82100.pdf. last access 9 February 2022.

Thompson, R.L., Smith, B.T., Grams, J.S., Dean, A.R., Broyles, C., 2012. Convective modes for significant severe thunderstorms in the contiguous United States. Part II: Supercell and QLCS tornado environments. Wea. Forecasting 27, 1136–1154. https://doi.org/10.1175/WAF-D-11-00116.1.

Trapp, R.J., Tessendorf, S.A., Godfrey, E.S., Brooks, H.E., 2005. Tornadoes from squall lines and bow echoes. Part I: climatological distribution. Wea. Forecasting 20, 23–34.

Trapp, R.J., Weisman, M.L., 2003. Low-level mesovortices within squall lines and bow echoes. Part II: their genesis and implications. Mon. Weather Rev. 131, 2804–2823.

Wallace, J.M., Hobbs, P.V., 2006. Atmospheric Science: An Introductory Survey. Elsevier Academic Press, Amsterdam.

Weisman, M.L. and Klemp, J.B., 1982. The dependence of numerically simulated convective storms on vertical wind shear and buoyancy. *Monthly Weather Review*, **110**, 504–520. https://doi.org/10.1175/1520-0493(1982)110%3C0504:TDONSC%3E2.0.CO;2

Weisman, M.L. and Klemp, J.B., 1984. The structure and classification of numerically simulated convective storms in directionally varying wind shears. *Monthly Weather Review*, **112**, 2479–2498.

Weisman, M.L. and Klemp, J.B., 1986. Characteristics of isolated convective storms. In *Mesoscale meteorology and forecasting*, 331–358. American Meteorological Society, Boston, MA. https://doi.org/10.1007/978-1-935704-20-1_15

Weisman, M.L., Davis, C.A., 1998. Mechanisms for the generation of mesoscale vortices within quasi-linear convective systems. J. Atmos. Sci. 55, 2603–2622.

Zanini, M.A., Hofer, L., Faleschini, F., Pellegrino, C., 2017. Building damage assessment after the riviera del brenta tornado, northeast Italy. Nat. Hazards 86, 1247–1273. https://doi.org/10.1007/s11069-017-2741-6

Figure1

Click here to access/download;Figure;fig1_140mm.jpg

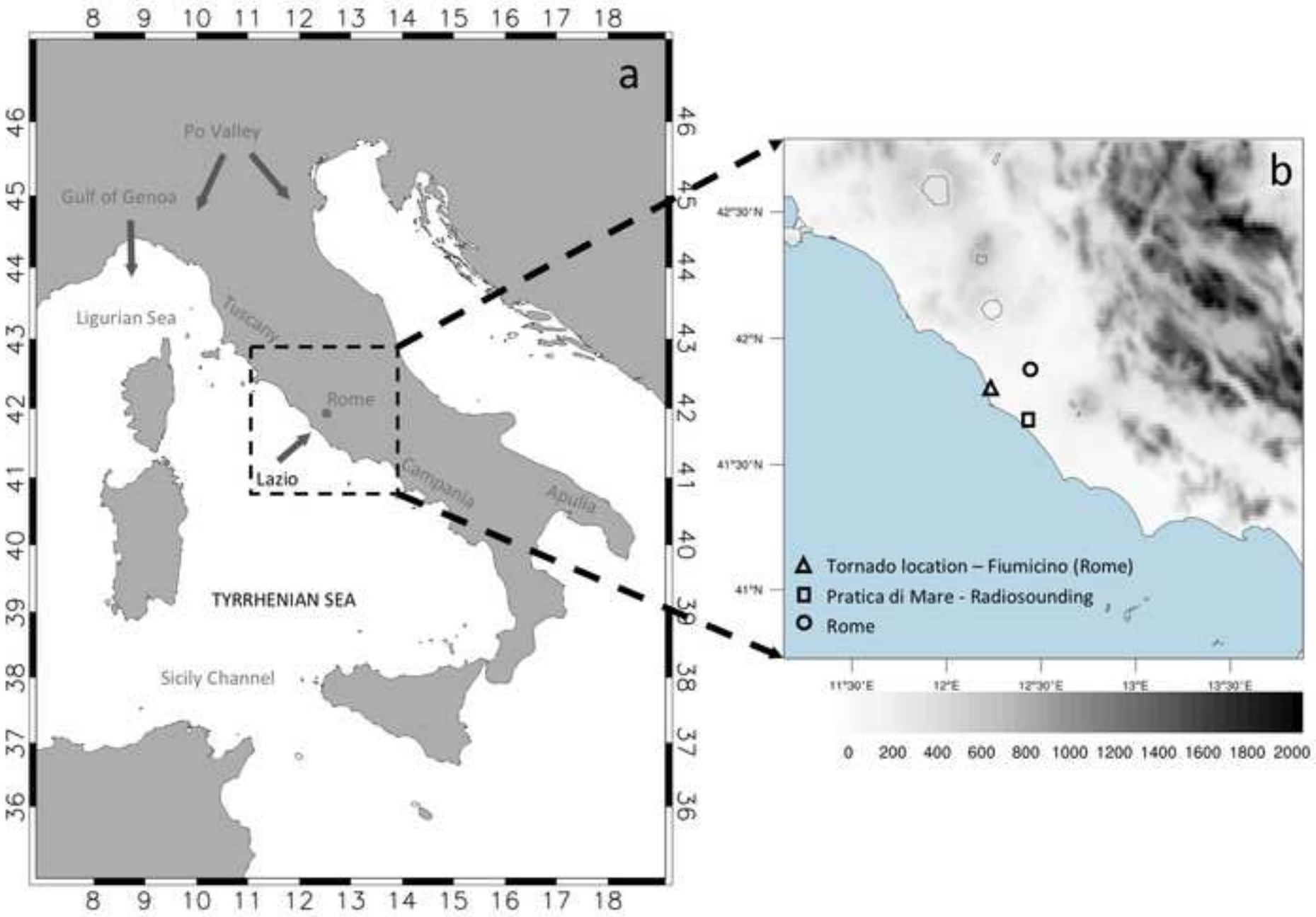

Figure2

Click here to access/download;Figure;fig2_90mm.jpg

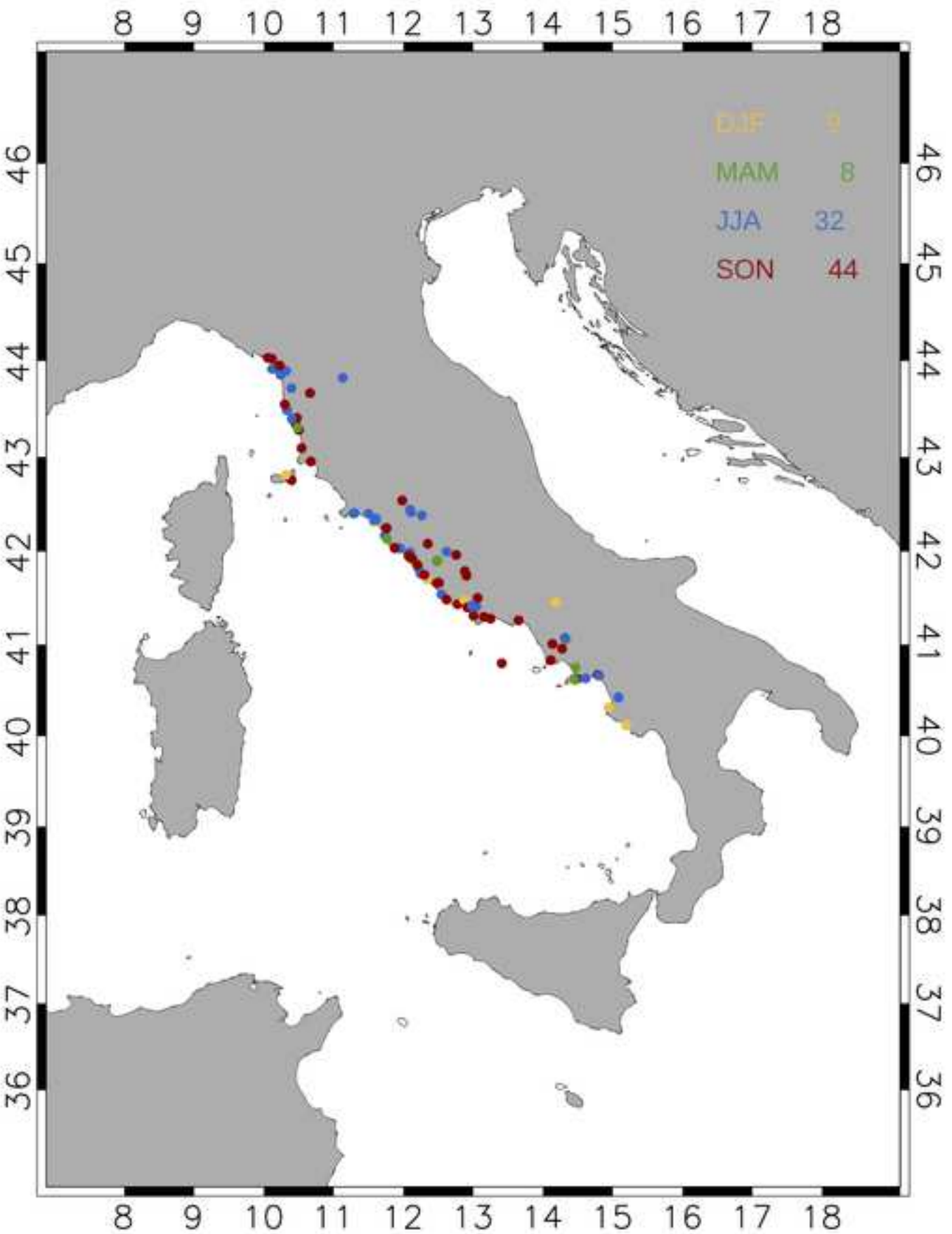

Figure3

Click here to access/download;Figure;fig3_140mm.jpg

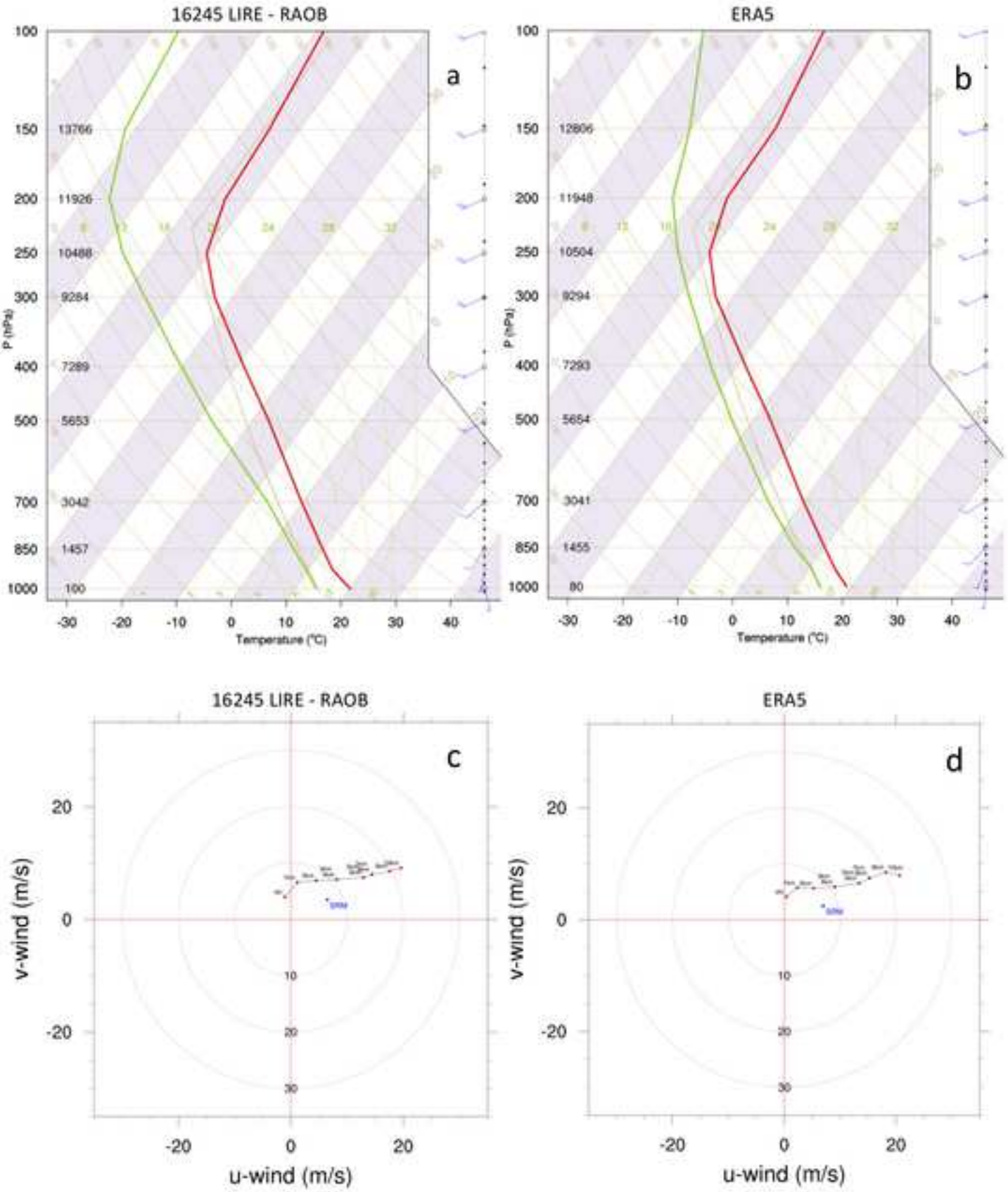

Figure4

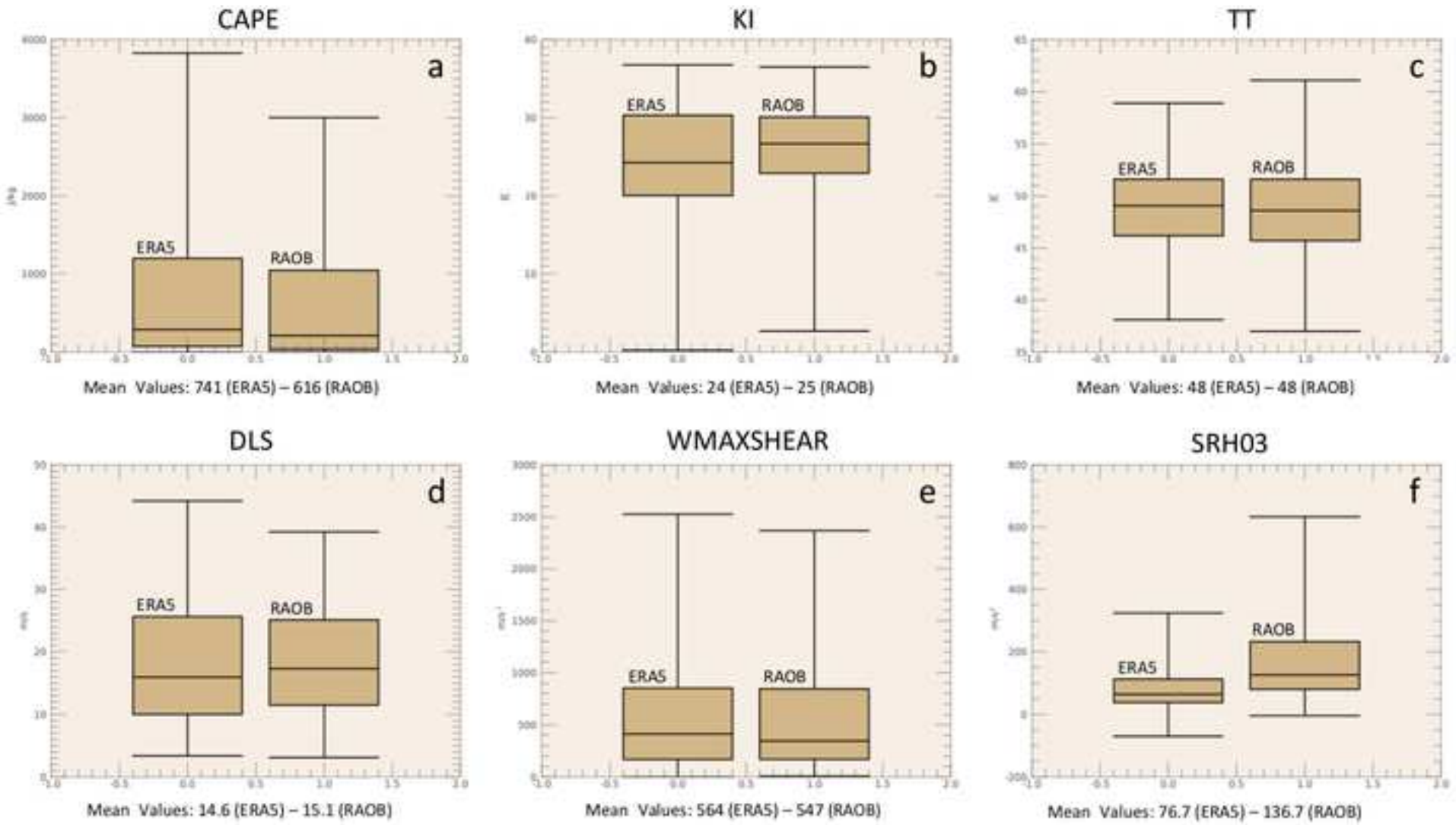

Figure5

Click here to access/download;Figure;fig5_190mm.jpg

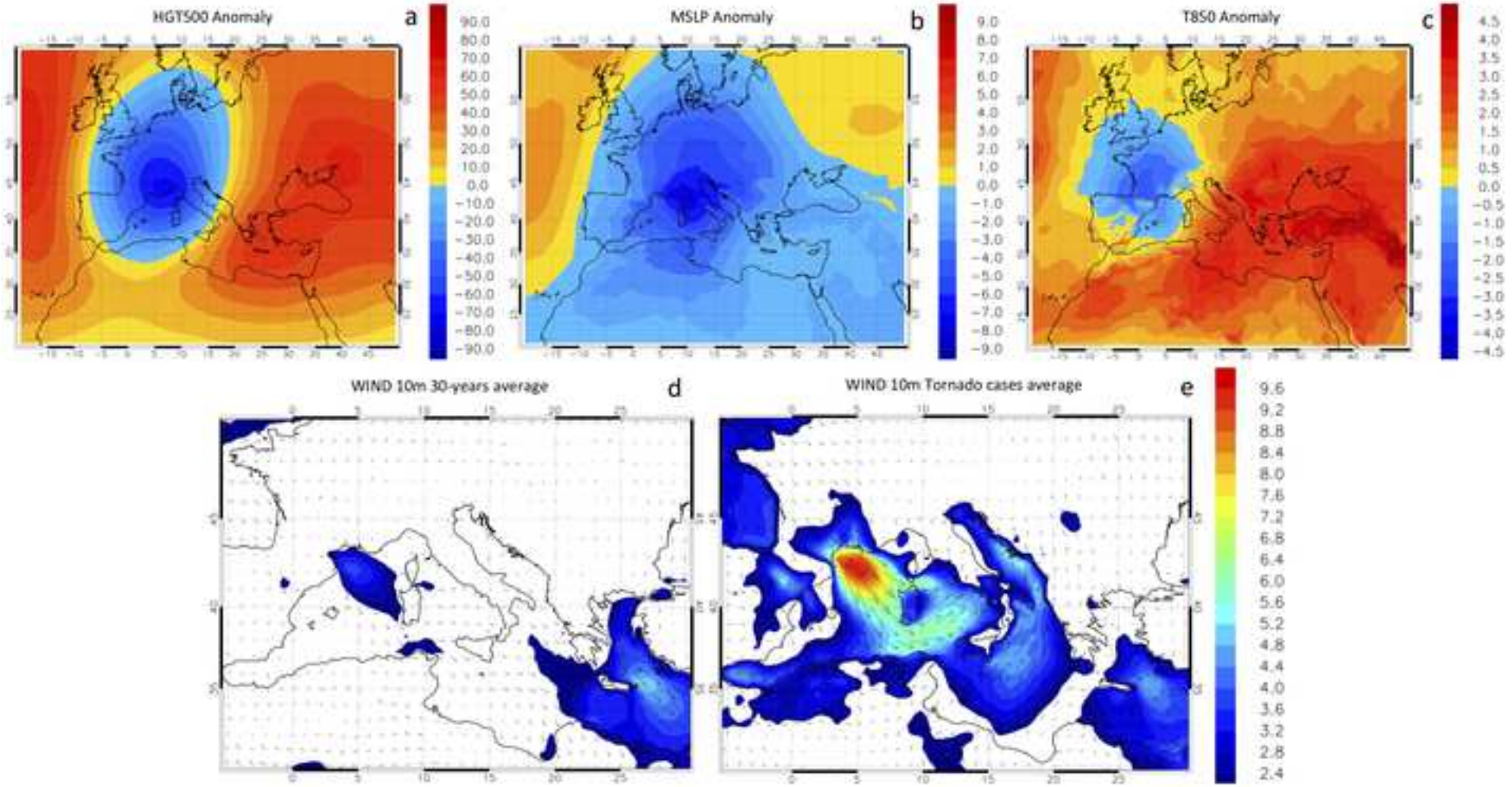

Figure6

Click here to access/download;Figure;fig6_140mm.jpg

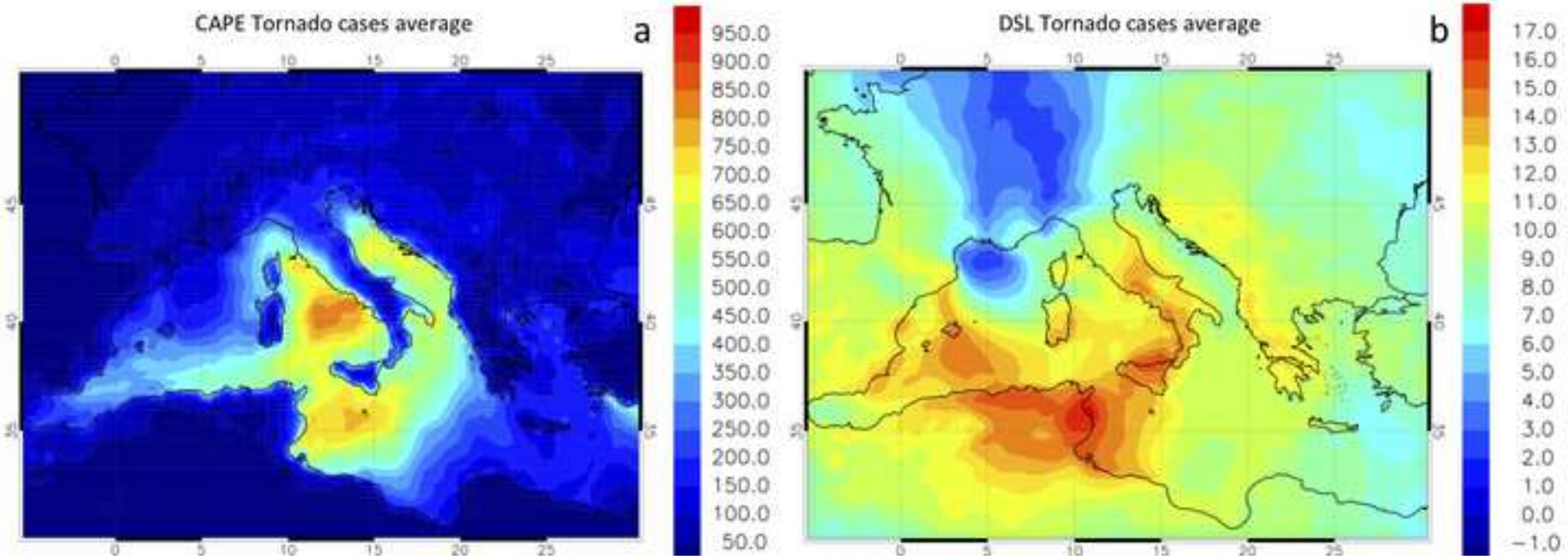

Figure7

Click here to access/download;Figure;fig7_140mm.jpg

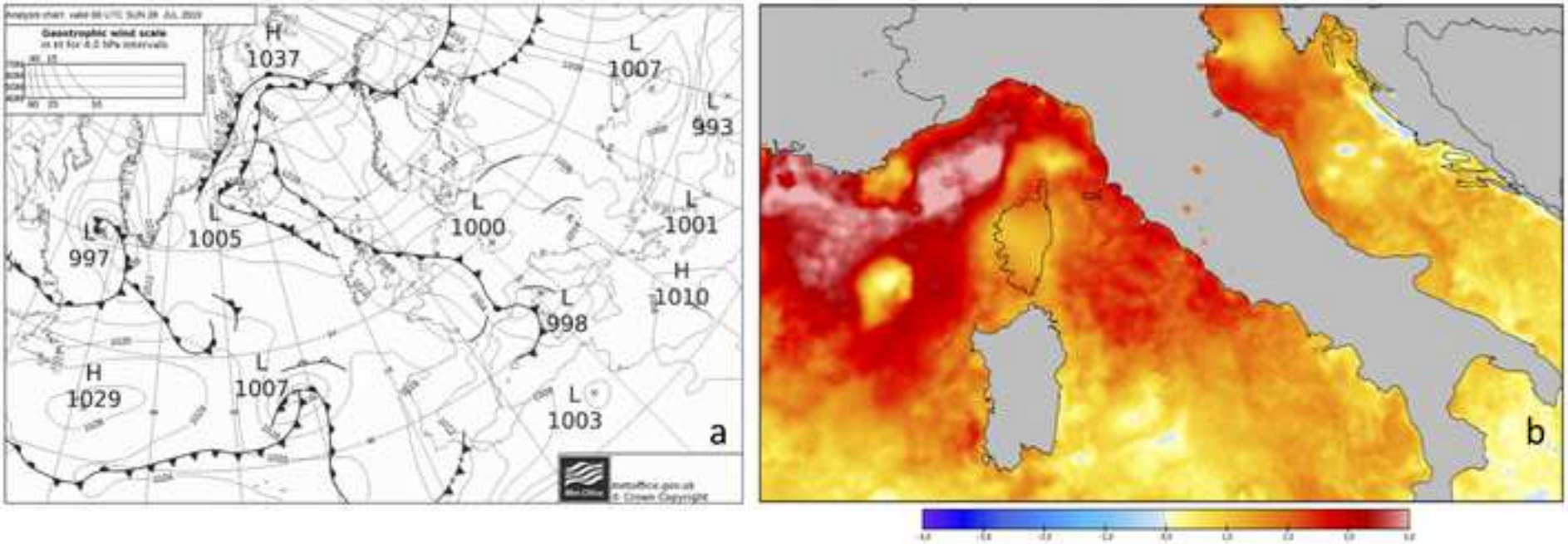

Figure8

Click here to access/download;Figure;fig8_140mm.jpg

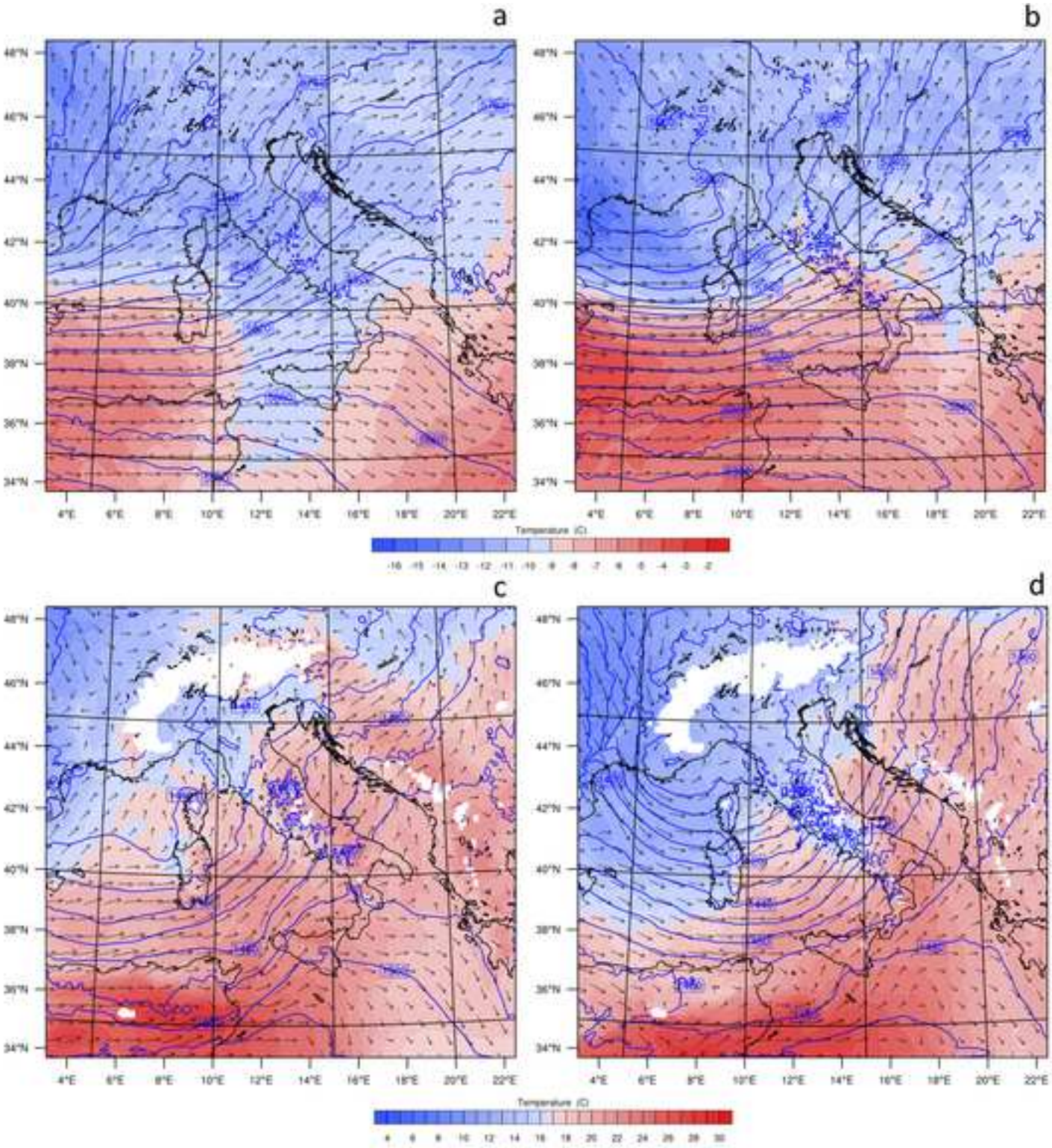

Figure9

Click here to access/download;Figure;fig9_190mm.jpg

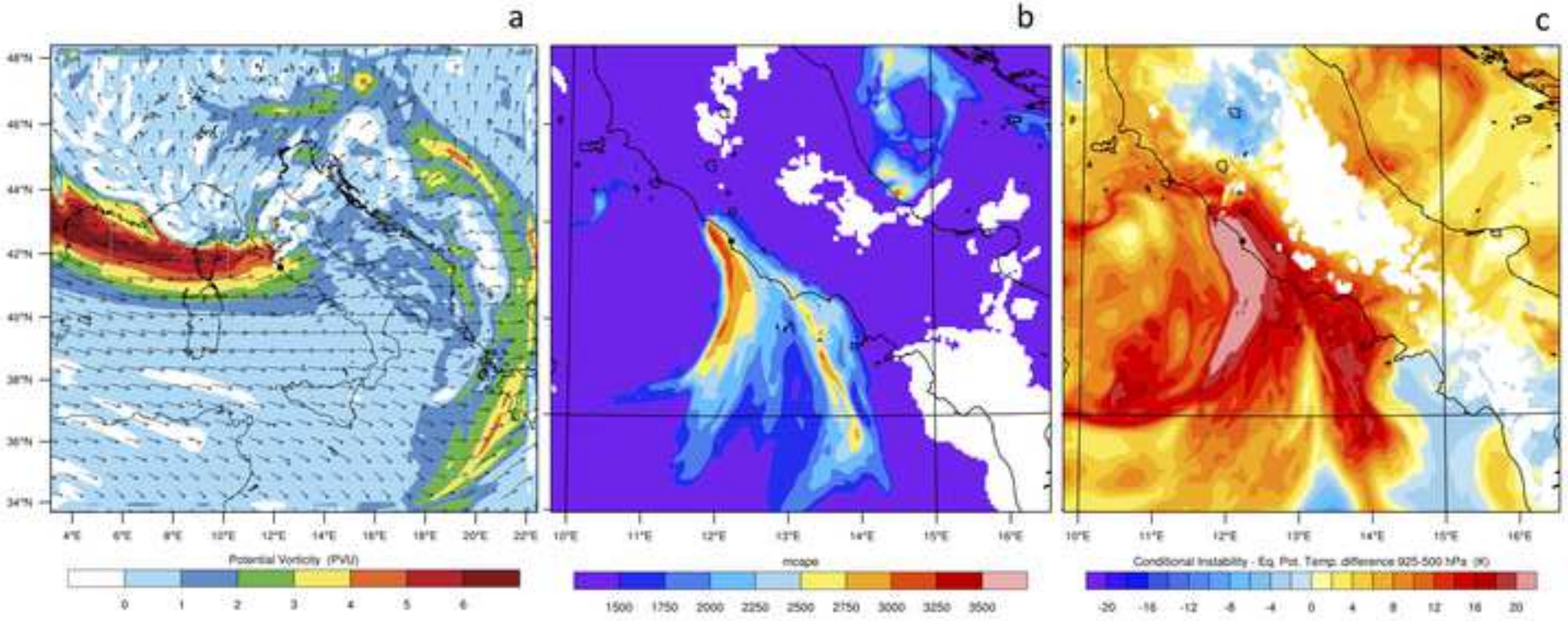

Figure10

Click here to access/download;Figure;fig10_140mm.jpg

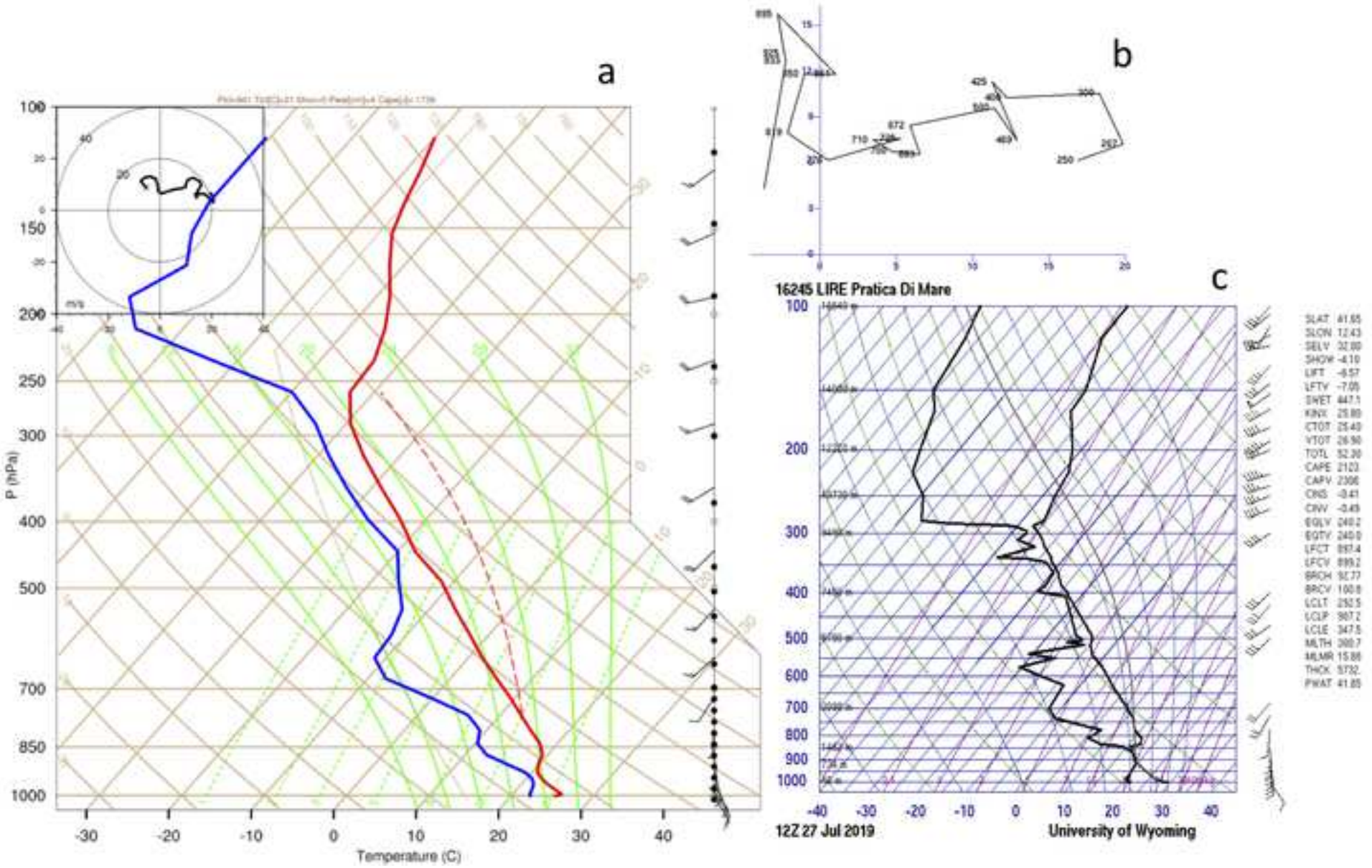

Figure11

Click here to access/download;Figure;Fig11_140mm.jpg

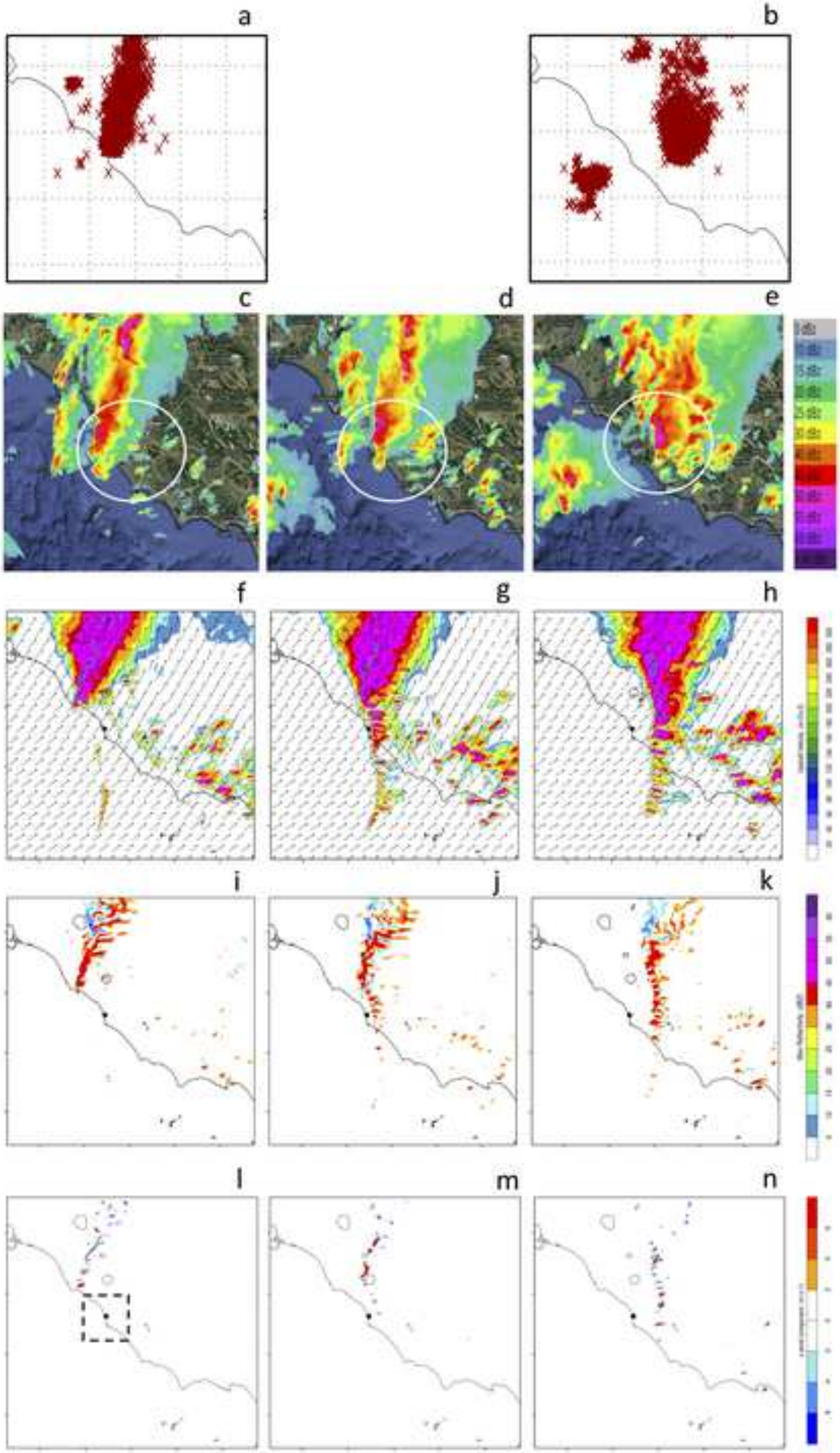

Figure12

Click here to access/download;Figure;fig12_90mm.jpg

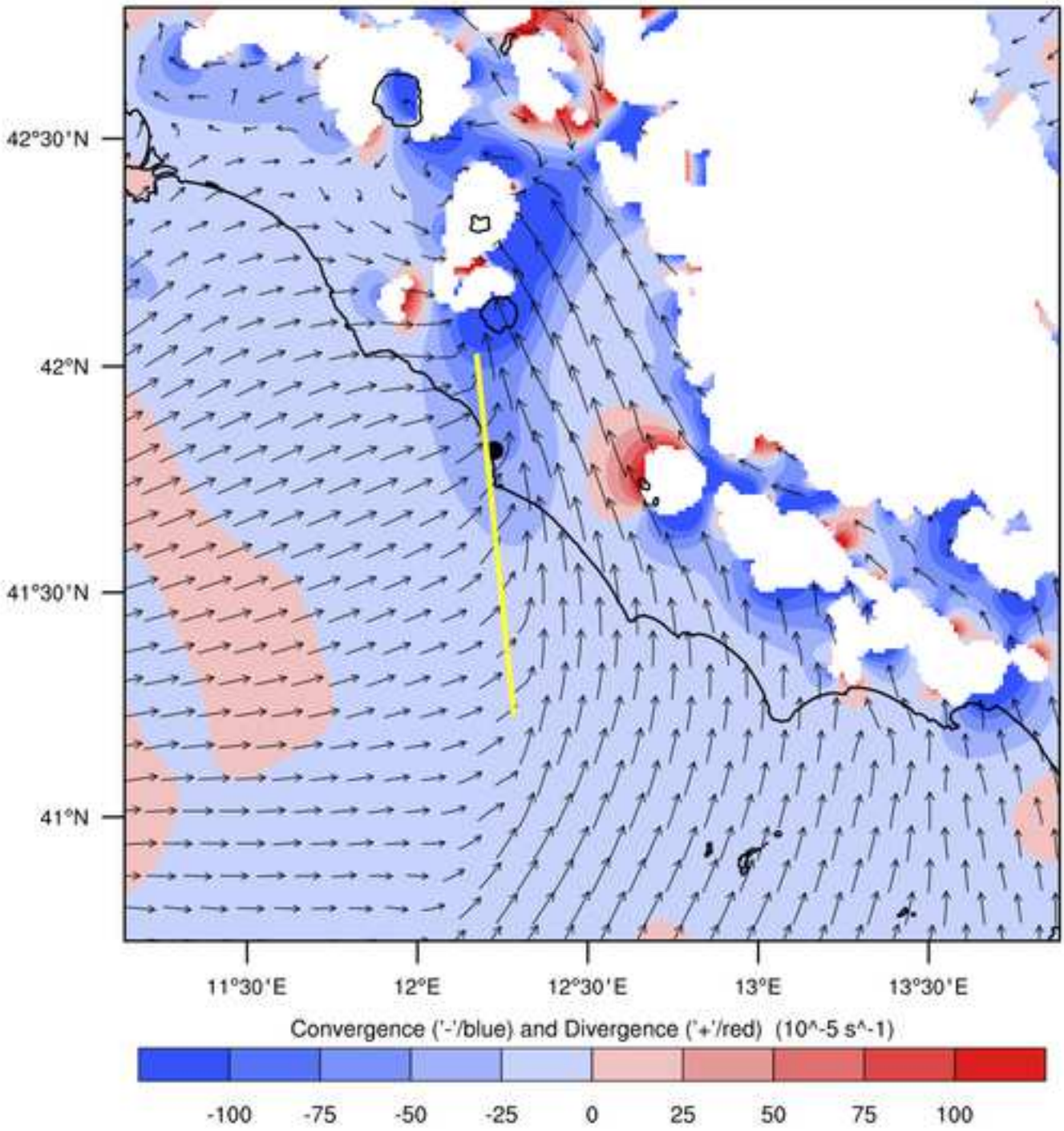

Figure13

Click here to access/download;Figure;fig13_140mm.jpg

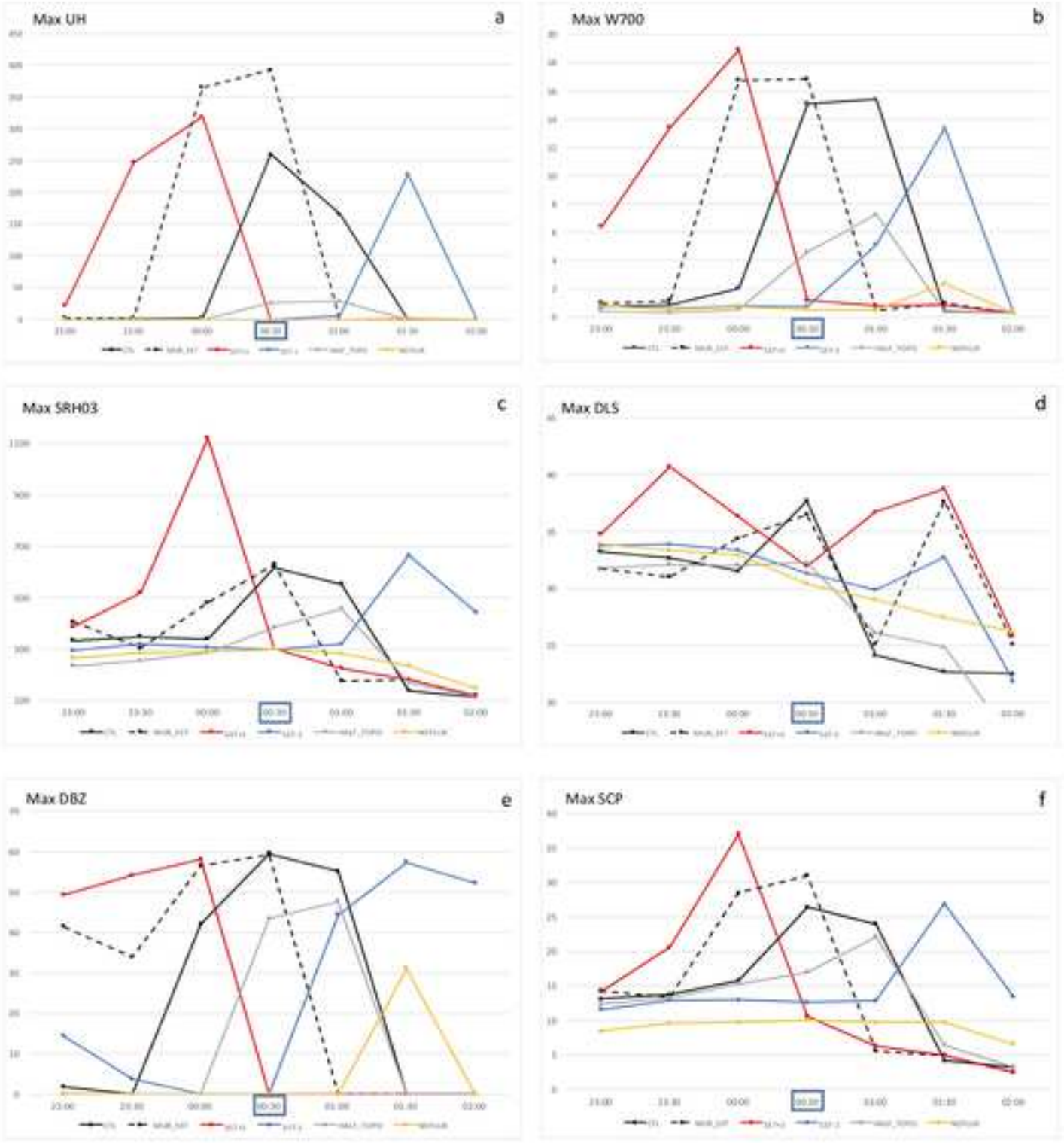

Figure_b1

Click here to access/download;Figure;fig_b1_90mm.jpg

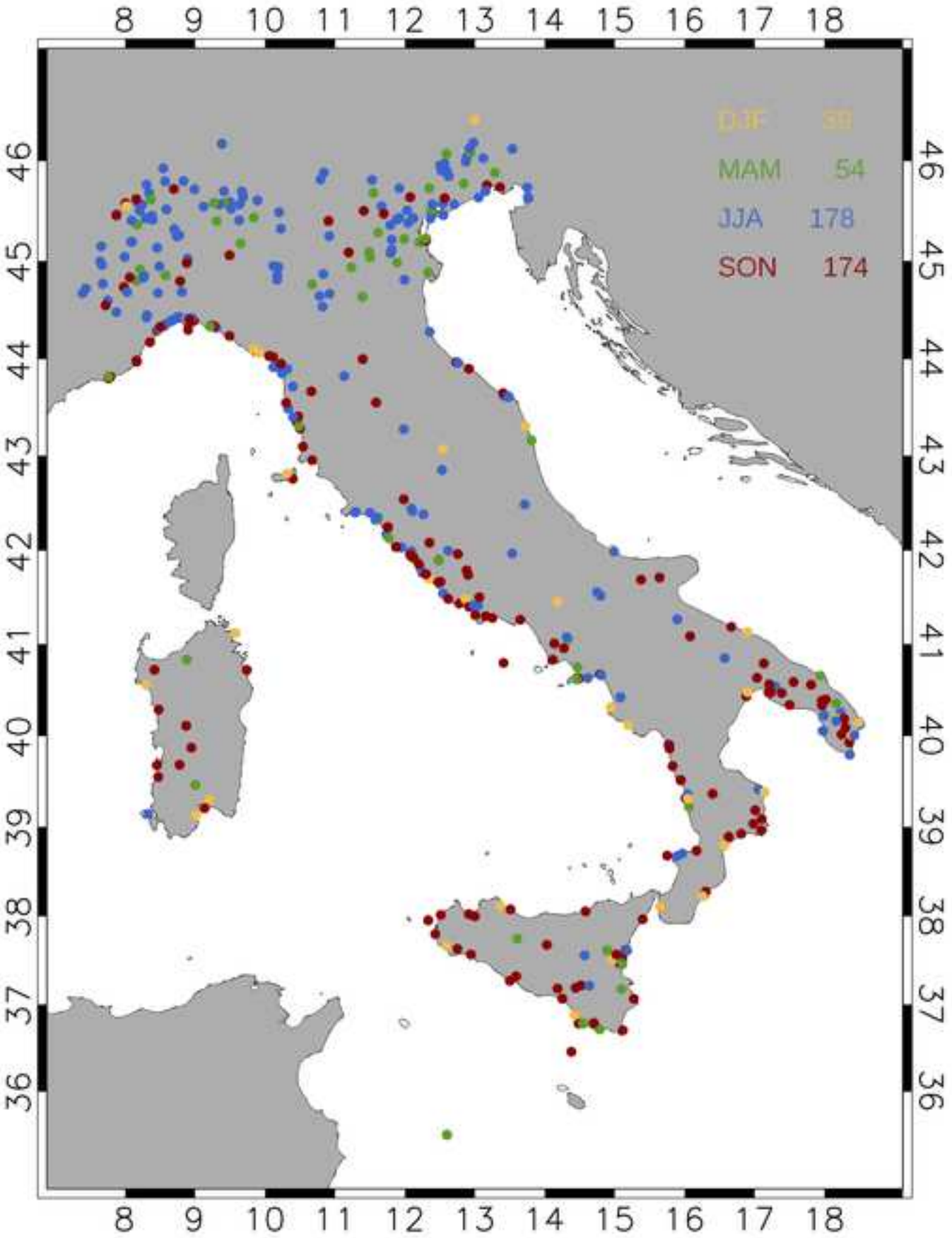

Figure_c1

Click here to access/download;Figure;fig_c1_140mm.jpg

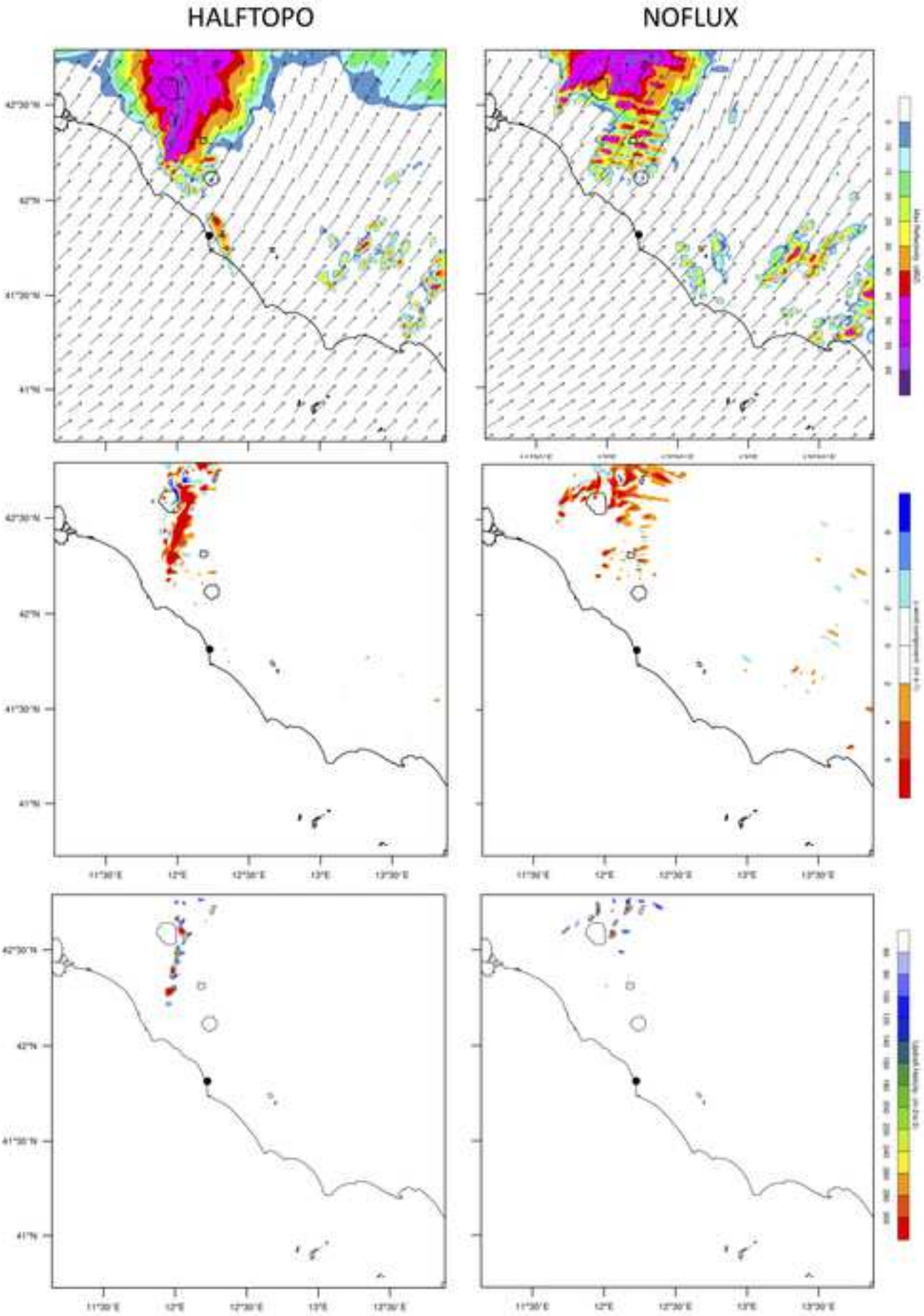

Figure_c2

Click here to access/download;Figure;fig_c2_140mm.jpg

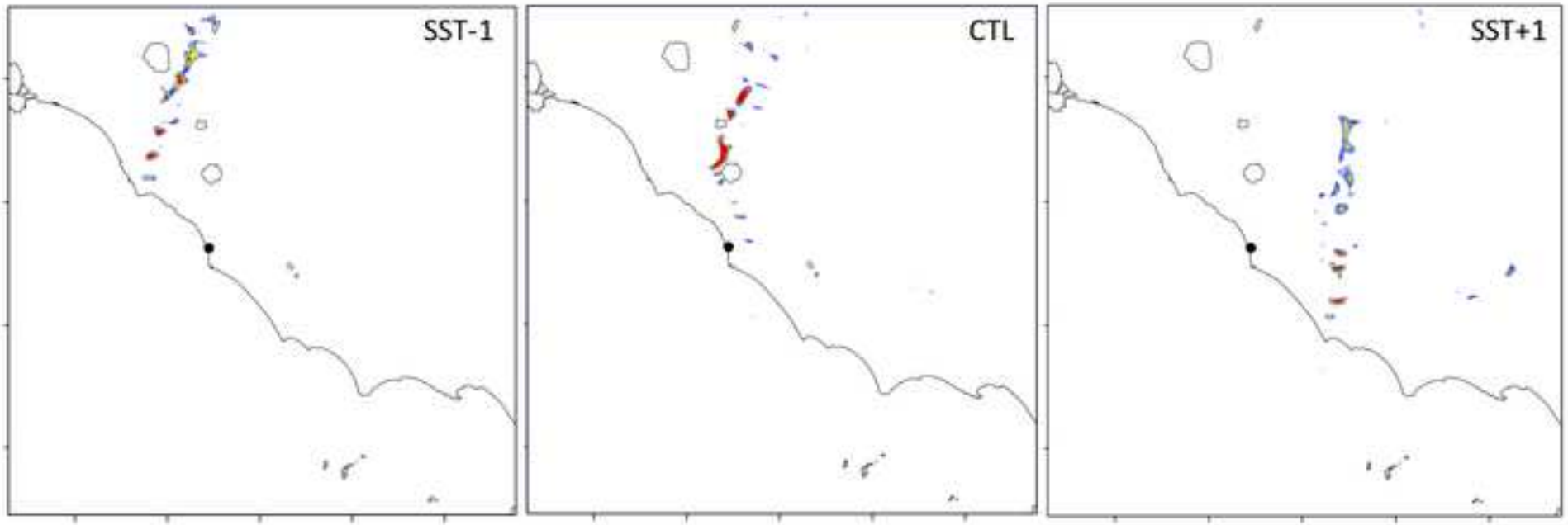

Declaration of interests

☒The authors declare that they have no known competing financial interests or personal relationships that could have appeared to influence the work reported in this paper.

☐The authors declare the following financial interests/personal relationships which may be considered as potential competing interests: